



저작자표시-비영리-변경금지 2.0 대한민국

이용자는 아래의 조건을 따르는 경우에 한하여 자유롭게

- 이 저작물을 복제, 배포, 전송, 전시, 공연 및 방송할 수 있습니다.

다음과 같은 조건을 따라야 합니다:



저작자표시. 귀하는 원저작자를 표시하여야 합니다.



비영리. 귀하는 이 저작물을 영리 목적으로 이용할 수 없습니다.



변경금지. 귀하는 이 저작물을 개작, 변형 또는 가공할 수 없습니다.

- 귀하는, 이 저작물의 재이용이나 배포의 경우, 이 저작물에 적용된 이용허락조건을 명확하게 나타내어야 합니다.
- 저작권자로부터 별도의 허가를 받으면 이러한 조건들은 적용되지 않습니다.

저작권법에 따른 이용자의 권리는 위의 내용에 의하여 영향을 받지 않습니다.

이것은 [이용허락규약\(Legal Code\)](#)을 이해하기 쉽게 요약한 것입니다.

[Disclaimer](#)

Master of Science

NANOSCALE THERMAL AND FLUID TRANSPORT PHENOMENON IN POROUS
MEDIA: A MOLECULAR DYNAMICS STUDY

The Graduate School
of the University of Ulsan

School of Mechanical Engineering

Mohammad Rashedul Hasan

NANOSCALE THERMAL AND FLUID TRANSPORT PHENOMENON IN
POROUS MEDIA: A MOLECULAR DYNAMICS STUDY

Supervisor: Dr. BoHung Kim

A Master's Thesis

Submitted to
the Graduate School of the University of Ulsan
In partial Fulfillment of the Requirements
for the Degree of Master of Science

by

Mohammad Rashedul Hasan

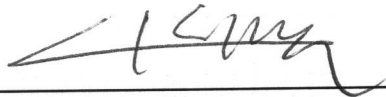
School of Mechanical Engineering

Ulsan, South Korea

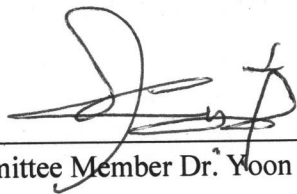
November 2019

NANOSCALE THERMAL AND FLUID TRANSPORT PHENOMENON IN
POROUS MEDIA: A MOLECULAR DYNAMICS STUDY

This certifies that the Master's Thesis
Of Mohammad Rashedul Hasan is approved.



Committee Chair Dr. Doo-Man Chun



Committee Member Dr. Yoon Ho Lee



Committee Member Dr. BoHung Kim

School of Mechanical Engineering
University of Ulsan, South Korea

November 2019

Abstract

Nanoscale Thermal and Fluid Transport Phenomenon in Porous Media: A Molecular Dynamics Study

(November 2019)

Mohammad Rashedul Hasan

The small length scales and large specific surface areas associated with the nanostructures play a key role in the molecular level thermal and fluid transport. In such nanometer length scales, the local intermolecular interaction creates temperature discontinuities between the solid-like interfaces and their neighboring fluid molecules. This phenomenon often referred to as interfacial thermal resistance (i.e., Kapitza resistance) during nanoscale thermal transport. There is also evidence that the fluid molecules are absorbed by the wall molecules promoting structural ordering of fluid at the solid/fluid interface. The local dynamic properties of this fluid layered structure are substantially different from the fluid properties at macroscale. Therefore, the continuum transport theories break down near the material interfaces at nanoscale.

In this thesis, we investigate the unique transport behaviors of fluid molecules in confining nanoenvironments using Molecular Dynamics (MD) simulations. Firstly, heat transfer across an interface between a monolayer coated solid substrate and fluid has been analyzed by varying the atomic mass (m_M) and interaction energy between monolayer molecules (ϵ_{MM}). In that case, the mutual combination of atomic mass (m_M) and interaction energy (ϵ_{MM}) of monolayer lead to a significant influence in heat transport at the interfacial region. It was found that Kapitza resistance monotonically increases with the increase of m_M

irrespective of ε_{MM} without any further change in the fluid-structure near the solid surface. This indicates the vibrational coupling between the molecules at the solid/fluid interface largely depend on the mass of monolayer molecules.

We also investigate the pressure-driven transport mechanism of liquid argon through nanoporous graphene membrane (NPGM) using MD simulations. In this study we check the validity and limitations of the assumptions of continuum flow equation. We present a thorough characterization of the density and pressure distribution of liquid argon based on the respective flow region to elucidate the unique fluid transport behaviors. The argon velocity adjacent to the pore edge was found lower than pore center suggesting the influence of the interaction between argon and carbon molecules at the pore boundary. In that case, we consider the argon velocity closest to the pore edge as slip velocity, which provides an update in the continuum flow equation. The local viscosity was also calculated from the thin argon film flows sheared by graphene walls. Our study shows that the entrance interfacial pressure and higher local viscosity in the vicinity of graphene membrane associated with the optimized definition of wall/fluid boundary near the pore edge play a critical role for the permeation of argon through NPGM.

Acknowledgements

I would like to express my sincere gratitude to my academic advisor Professor BoHung Kim to give me an opportunity in his world-class research group. His guidance, patience and continuous encouragement tremendously help me to improve my research skills. I am extremely thankful for his time and support which eventually build the foundation of my research carrier. I will always bear in mind his moral and ethical guidelines till the rest of my life. I truly respect his personality and hope to become an independent researcher as good as Professor BoHung Kim.

I am also very grateful to Dr. Truong Quoc Vo for his invaluable help in the nanoscale heat transfer project. I feel very fortunate to work with him. His insightful suggestions, while writing the manuscript, really helped me a lot in the beginning of my study on Molecular Dynamics Simulations.

I really appreciate the research work done by all of the MNTF lab members. Their quality of work always motivates me to move forward and never give up. Yechan, Emily and Gyoung Hun were always very friendly and helpful to me. I also had a great time with Jaber, Masud, Ehsanul, Seonghwan, Shihab and Prince. I would like to specially appreciate Dr. Mahbubul Alam Shoaib, Dr. Shahed Uddin Ahmed Shazib, and Dr. Farman Ullah for their valuable suggestions. It has been a wonderful experience for me to meet with these highly respected personalities during my study in the University of Ulsan.

This thesis is dedicated to my beloved parents, Mohammad Nur Nabi and Shahnaj Begum. They made an enormous sacrifice in their life to make my life better. I am nothing without them. I am very grateful to almighty Allah for being a child of my parents.

Table of contents

Abstract.....	iv
Acknowledgments.....	vi
Table of contents.....	vii
List of Figures.....	ix
List of Tables.....	xi
Chapter 1. Introduction.....	xii
Chapter 2. Manipulating Thermal Resistance at Solid–fluid Interface through Monolayer Deposition.....	4
2.1. Abstract.....	4
2.2. Introduction.....	4
2.3. Theoretical Background.....	7
2.4. Result and Discission.....	12
2.4.1. Effect of monolayer on interfacial heat transfer.....	12
2.4.2. Role of monolayer mass and interaction energy.....	14
2.4.2.1. Impact on Kapitza Length.....	14
2.4.2.2. Impact on Density profiles.....	16
2.4.2.3. Impact on Vibrational Density of States.....	18
2.4.3. Effect of thermal oscillation frequency on the Kapitza length.....	20
2.5. Conclusion.....	22
Chapter 3. Nanopore Flow Modeling for the Transportation of Argon through Nanoporous graphene membrane.....	24
3.1. Abstract.....	24
3.2. Introduction.....	24
3.3. Theoretical Background.....	29
3.4. Molecular Dynamics Simulations.....	30
3.5. Result and Discission.....	34
3.5.1. Characterization of fluid dynamics properties based on respective flow region.....	34
3.5.1.1. Density distributions of liquid argon in the vicinity of graphene membrane.....	34

3.5.1.2. Pressure distributions of liquid argon in the vicinity of graphene membrane	35
3.5.1.3. Effect of nanoconfinement on local viscosity	39
3.5.1.4. Slip velocity inside graphene nanopore	43
3.5.2. Comparison of continuum and molecular–level transport properties correlated with the definition of wall/liquid boundary near the pore edge	45
3.6. Conclusion	49
Chapter 4. Conclusions.....	51
References.....	53

List of figures

Figure 2.1. (a) Snapshot of the MD simulation of heat transfer at the interface between the monolayer-coated solid surface and argon. (b) Velocity distribution for $m_M = 12m_F$ and $\varepsilon_{MM} = 10\varepsilon_{FF}$ at the NEMD steady state condition compared to the Maxwell-Boltzmann distribution function at (left) one-atomic-layer in the left wall, (middle) fluid argon in the bulk region, and (right) interfacial monolayer on the right wall.

Figure 2.2. Typical temperature profiles across the wall-fluid interface **(a)** without and **(b-d)** with monolayer coated for $\varepsilon_{MM} = 10\varepsilon_{FF}$ at various values of m_M

Figure 2.3. Dependence of thermal oscillation frequency between monolayer and fluid on thermal conductivity (Black line represents the value for λ without monolayer coating)

Figure 2.4. Variation of $L_{K,r}$ as a function of (a) m_M at different $\varepsilon_{MM}/\varepsilon_{FF}$ and (b) $\varepsilon_{MM}/\varepsilon_{FF}$ at different m_M

Figure 2.5. Density profiles near the hot wall for (a) $\varepsilon_{MM} = 10\varepsilon_{FF}$ at various values of m_M and for (b) $m_M = 12m_F$ at various values of ε_{FF}

Figure 2.6. VDOS of wall, monolayer and fluid argon atoms as a function of frequency for $\varepsilon_{MM} = 10\varepsilon_{FF}$ at different values of m_M . **(a)** Interface without monolayer coating: surface atoms in fluid (green line), innermost substrate (red line) and bulk substrate (brown line). **(b)-(f)** Interface with monolayer coating: surface atoms in fluid (green line), monolayer (red line), innermost substrate (blue line) and bulk substrate (brown line). The grey area illustrates the overlap between VDOS

Figure 2.7. VDOS of innermost wall and monolayer atoms for $m_M = 10m_F$ at different values of ε_{MM}

Figure 2.8. “Master” curve describing the variation of the Kapitza length at the interface between fluid argon and monolayer-coated solid substrate as a function of oscillating frequency

Figure 3.1. (a) Schematics of the flow of liquid argon through nanoporous graphene membrane, (b) Physical description of specular reflection wall, and (c) Insight of graphene pore with three probable pore boundary

Figure 3.2. Density distribution of argon along with axial direction of flow within $a_{cc} = 1.10925$ nm pore radius

Figure 3.3. Pressure distribution of argon along the axial direction of flow within $a_{cc} = 1.10925$ nm pore radius at $U_w = 1.5$ m/sec,

Figure 3.4. Pressure distribution with, (a) kinetic term and (b) virial term, along z axis within $a_{cc} = 1.10925$ nm pore radius at $U_w = 1.5$ m/sec

Figure 3.5. Variation of pressure difference between front and back reservoirs in the bulk and interface region respectively with the increase of U_w

Figure 3.6. (a) Schematics of MD simulation of liquid argon sheared by graphene walls, (b) Velocity distribution of liquid argon along the z- direction of the channel, and (c) Shear stress component (S_{xz}) of liquid argon compared with density distribution from nanopore flow simulation

Figure 3.7. Distribution of (a) the shear rate ($\dot{\gamma} = \frac{dv_x}{dz}$) and (b) Local viscosity of liquid argon as a result of the sheared driven flow by the graphene walls

Figure 3.8. 3D averaged argon velocity profile in the radial direction (xy- plane) within $a_{cc} = 1.10925$ nm pore radius at $U_w = 3.5$ m/sec

Figure 3.9. Argon velocity profile in the nanopore within $a_{cc} = 1.10925$ nm pore radius at $U_w = 1.5$ m/sec

Figure 3.10. Comparison of velocity profile from NEMD simulations and modified Sampson flow equation within $a_{cc} = 1.10925$ nm pore radius by varying pressure difference in bulk and

interface region (a-b) with bulk viscosity, and (c-d) with interface viscosity at $U_w = 1.5$ and 3.5 m/sec

Figure 3.11. Comparison of velocity profile from NEMD simulations and modified Sampson flow equation for three probable pore boundary with ΔP_{peak} and μ_{int} at $U_w = 1.5$ m/sec. Data is obtained for $a_{cc} = 1.10925$ nm pore radius

Figure 3.12. Comparison of velocity profile from NEMD simulations and modified Sampson flow equation for the pore boundary at L'' with ΔP_{peak} and μ_{int} . Each line and circle symbol profile with same color (from bottom) represents the data for $U_w = 1.0, 1.5, 2.0$ and 2.5 m/sec respectively. Data is obtained for $a_{cc} = 1.10925$ nm pore radius

List of tables

Table 2.1. Interaction parameters studied in the simulation domain

Table 3.1. Details of the interaction parameters utilized in this study

CHAPTER 1

INTRODUCTION

The behavior of fluids at solid-fluid interfaces plays an important role in various technical processes such as heat transfer, coating, adhesion etc. In recent years, with the advancement of modern technologies, many Micro and Nano Electro-Mechanical Systems (MEMS/NEMS) have been developed with high accuracy and sensitivity. Most importantly, the heat and mass transport phenomena in these MEMS/NEMS devices are quite different from those at macroscale. In such cases, understanding the physics of fluid flows at solid-fluid interfaces is critical to designing, fabricating, utilizing and optimizing these nanoscale device components.

It has been noted that fluid-wall interactions are substantially different from classical fluid transport mainly due to the size effects of the nano-conduits geometries. Consequently, this creates interfacial thermal resistance (i.e., Kapitza resistance [1] and slip effect [2] at the solid/liquid interface. In that case, surface chemistry of the solid surface, for example, crystal structure [3] (face-centered cubic, body-centered cubic etc.), physical property of the solid molecule [4] (strong or weak wetting), surface roughness or smoothness [5,6], surface coating [7–9], surface thickness [10], changing surface temperature [11] and pressure [12], nano-engineering the solid substrate [13] etc. is the key factors determining the heat and mass transport mechanism at molecular level. Moreover, the liquid molecules form a solid-like layering structure over several atomic distances from the solid wall which is observed by both experimentally [14,15] and numerically [16]. The dynamics of this fluid layered structure also produce a different shear rate and viscosity at the wall/fluid boundary than the bulk flow region [17,18]. These decisive effects of the molecular structure of the solid wall and fluid molecules, as well as their interactions, play a critical role in nanoscale fluid dynamics.

Therefore the traditional continuum model breaks down at the materials interfaces [19]. The findings, in this thesis, have identified the limitations in modeling/predicting the fluid behaviors in molecular fluidic devices.

Molecular dynamics (MD) simulation is a promising approach to investigate nanoscale phenomena. Therefore, I perform equilibrium and non-equilibrium molecular dynamics simulation using LAMMPS [20] to understand the behavior of fluid particles at the solid/fluid interface and the effect of interfacial fluid dynamics properties on heat and mass transport. In this method, the dynamics parameters of particles (i.e., position, velocity, and intermolecular force) can be determined by solving Newton's second law as follows,

$$F = m \frac{d^2 r}{dt^2} \quad (1)$$

where F is the sum of the forces acting on the particles by the other particles in the system, r is the position vector of the particle, t is the time, and m is the mass of the particle. The velocity of the molecule can be obtained by integrating the equation 1. Further integrating the velocity term, results in its displacement. Therefore, step by step integration of equation 1 for every particle from the random initial configurations, computed from the Boltzmann distribution, provides the trajectory of the movement of every particle in the simulation domain. The information from the simulated trajectory of each particle can be further processed by time-averaging, ensemble averaging, or both. Finally, the averaged MD data provide macroscopic physical properties (i.e., density profile, velocity profile, temperature profile, etc.) over the entire simulation domain.

The thesis is organized as follows. In chapter 2, I investigate the heat transfer across an interface between a monolayer coated solid substrate and fluid. The effect of the monolayer on interfacial thermal resistance (i.e., Kapitza resistance) was studied by varying

its atomic mass (m_M) and interaction energy between monolayer particles (ϵ_{MM}). The effect of the monolayer on the Kapitza resistance was also summarized by a fourth polynomial function that demonstrates the contribution of both m_M and ϵ_{MM} with respect to each other on the Kapitza resistance.

In chapter 3, I investigate the pressure-driven transport mechanism of liquid argon through nanoporous graphene membrane. In this study, I investigate fluid dynamics properties such as density, pressure variation and viscosity depending on the flow region. The results indicate that the continuum transport theory, i.e., Sampson flow equation, fails to predict the argon flow velocity profile inside graphene nanopore. It was found that fluid layering in the vicinity of the graphene membrane plays a critical role in nanoscale fluid transport mechanism. Because, the fluid layering effect at the solid/fluid interface induces significantly higher density, pressure, and viscosity than the bulk flow region of the simulation domain. Moreover, slip velocity of argon adjacent to the pore edge was measured, which provides an update in the Sampson flow equation. Finally, the modified Sampson flow equation was analyzed with the characterized fluid dynamics properties based on the respective flow region and effective pore boundary to accurately predict the argon velocity profile inside the graphene nanopore.

CHAPTER 2

Manipulating thermal resistance at the solid–fluid interface through monolayer deposition

This material presented in this chapter was published in 2019 in issue 9, pages 4948-4956, of the RSC Advances. DOI: 10.1039/C8RA08390H

2.1. Abstract

Heat transfer across an interface between the monolayer coated solid substrate and fluid has been extensively analyzed through a series of non-equilibrium molecular dynamics simulations. The effect of monolayer was studied by varying its atomic mass (m_M) and interaction energy between monolayer particles (ϵ_{MM}). Even though the fluid adsorption is playing a role in heat transfer at the solid–fluid interface, we found that the interfacial thermal resistance (Kapitza resistance) is highly affected by the insertion of monolayer without any further change in the liquid structure near the solid surface. Kapitza length monotonically increases with the increase of m_M irrespective of ϵ_{MM} . The observations were explained by analysis of the overlap of phonon spectrum at the interface using vibrational density of states. The effect of monolayer on Kapitza length was summarized by a fourth polynomial function that demonstrate the contribution of both m_M and ϵ_{MM} with respect to each other on the Kapitza resistance within the parametric range studied.

2.2 Introduction

Thermal transport through an interface between two dissimilar materials is known to result in a temperature jump ΔT . The ratio of this temperature jump to the rate of heat transfer (Q) determines the interfacial thermal resistance (Kapitza resistance; i.e., $R_K = \Delta T/Q$) [1]. Therefore, R_K plays a key role in controlling heat dissipation at the interfaces. As with

the concept of velocity slip length when fluid passes to solid surfaces [21], thermal resistance length (L_K , known as Kapitza length) can be defined by extrapolating the temperature profile from fluid into the solid. Consequently, Kapitza length is defined as the equivalent thickness of fluid at the solid–fluid interface, with the same temperature gradient of the respective fluid region, that causes equivalent thermal resistance on the interface [16]. If the Fourier law ($Q = -\lambda \nabla T$) is valid with constant thermal conductivity λ , then the Kapitza length can be estimated as

$$\Delta T = L_K \left. \frac{\partial T}{\partial n} \right|_{\text{liquid}}, \quad (1)$$

where $\partial T / \partial n$ is the temperature gradient on the fluid side in the direction (z-axis) of heat transfer.

Recent developments in nanoscience and technology have attracted a vast number of investigations of mass, momentum, and energy transport in nanoscale structures, and nanoconduits [22,23]. Several methods have been used to manipulate the Kapitza resistance, such as, changing the pressure of the nano–confined fluid [24,12], using different solid lattice orientations [25,26], changing the wall temperature [11,27], inserting metallic nanoparticles into the fluids (i.e., nanofluids) [28,29], nanoengineering the solid substrate [30–33]. However, wall–fluid interaction energy, which solely determines the surface wettability [34–36], is the key factor affecting the Kapitza resistance. Increasing intermolecular interaction strength at the interface (i.e., enhancing the wetting degree) reduces the interfacial thermal resistance and vice versa [11,16,17,37–42]. In case of nanoparticle–fluid interfaces, Tascini et al. also showed that large interfacial curvature (nanoparticle size) coupled with strong nanoparticle–fluid interaction strength provide optimum heat transport near the interfacial region [43]. Moreover, in 2016, Ge *et al.* used time–domain thermoreflectance to measure the

Kapitza length between water and various solids through the transport of thermally excited vibrational energy across the interfaces [44]. It was reported that the Kapitza length at hydrophobic interfaces (10–12 nm) is a factor of 2–3 larger than the Kapitza length at hydrophilic interfaces (3–6 nm). Nevertheless, changing solid substrate material seems inapplicable, because every device has its own specific application and usage and operating conditions.

For such a case, using two-dimensional (2D) material coated on solid substrate has become a potential solution because one atom thick layers of almost any material are transparent to visible light; however, this can vary the energy transport at the interface. Since the discovery of graphene in 2004 [45], it has become a cutting-edge material; that opens up a Pandora's box for other 2D materials that might be beyond the limited current applicability of graphene. Recently, 2D materials have been attracting increasing attention due to the many interesting properties originating from bulk to monolayer transition [46,47]. For instance, Rafiee *et al.* measured a 30-40% increase in condensation heat transfer as a result of the ability of graphene coating to suppress copper oxidation [48]. The enhancement of condensation heat transfer performance with graphene coatings was also confirmed in the report of Preston *et al.* [49]. More recently, the results on Kapitza resistance revealed that the interfacial temperature jump increases with the introduction of graphene at the interface between solid and fluid water [8,19,50]. Meanwhile, the dominant influence of monolayers WS₂ and MoS₂ on the wettability of the underlying substrates has also been investigated [9]. It was shown that even when a monolayer WS₂ (or MoS₂) is coated, the measured contact angle highly increases compared to the substrate without coatings.

For the reasons given above, a systematic study on the effects of monolayer coating on the interfacial heat transfer is required. There have been several studies on thermal

boundary resistance at the perfect interfaces between solids [51,52], and with the introduction of monolayer near the solid-solid interface [53,54]. However, they lack an investigation on the variation of Kapitza length at solid–fluid interfaces with the presence of monolayer inserted under a wide range of its atomic properties. Note that substrate and monolayer particles are likely to vibrate back and forth in both horizontal and vertical directions about a fixed lattice point unlike the fluid particles, as the interatomic potential is comparatively weak for fluids. In that case, the mutual combination of atomic mass (m_M) and interaction energy (ε_{MM}) of monolayer may lead to a significant influence in heat transport at the interfacial region. Therefore, in this paper, we aim to study the effects of the interfacial monolayer on Kapitza resistance between solid and fluid using molecular dynamics (MD) simulations by the variation of m_M and ε_{MM} . Finally, L_K under the effect of monolayer was compared as the function of m_M and ε_{MM} . It is known that interaction energy (ε) and mass (m) are related to the thermal oscillation frequency, which is proportional to $\sqrt{\frac{\varepsilon}{\sigma^2 m}} = \omega$ [38].

Hence, in this paper, we attempt to correlate L_K and $\omega_r = \frac{\omega_M}{\omega_F}$. Herein, ω_r denotes the interfacial mismatch at the solid–fluid interface, where ω_M and ω_F represents the thermal oscillation frequency of monolayer and fluid particles respectively.

2.3. Theoretical Background

The solid wall atoms are initially constructed in perfect FCC structure with a computational domain of $L_x = 8a$, $L_y = 8a$ and $L_z = 15a$ across each respective direction, where the lattice constant $a = 0.5256$ nm (see Figure 2.1). Fluid particles were confined between two solid walls with and without monolayer coating. The number density ($\rho = N\sigma^3/V$) of fluid was set to 0.8 at a distance of 10 nm along the z-direction. For simulations where

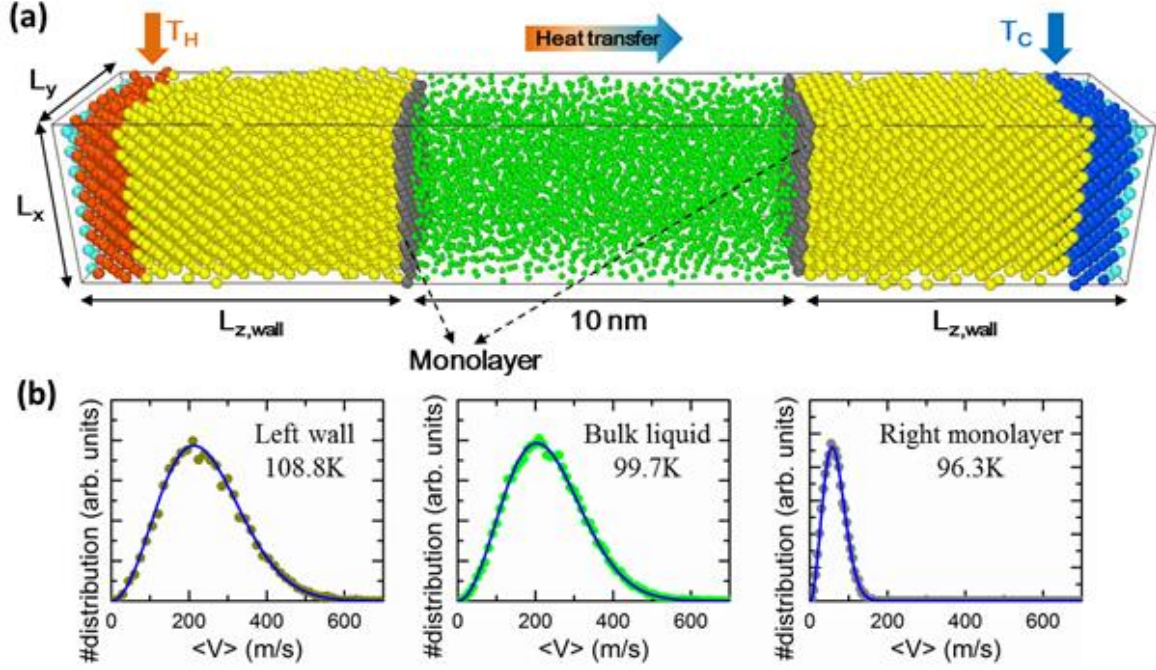


Figure 2.1. (a) Snapshot of the MD simulation of heat transfer at the interface between the monolayer-coated solid surface and argon. (b) Velocity distribution for $m_M = 12m_F$ and $\varepsilon_{MM} = 10\varepsilon_{FF}$ at the NEMD steady state condition compared to the Maxwell-Boltzmann distribution function at (left) one-atomic-layer in the left wall, (middle) fluid argon in the bulk region, and (right) interfacial monolayer on the right wall.

the interfacial monolayers (colored gray) are presented, the innermost solid layers, (i.e. the ones facing the fluid argon), are replaced by the monolayer. We limit the monolayer to the non-lattice-mismatch to the lattice structure of the solid walls, but with a different atomic mass and interaction energy depending on the cases studied. To perform the non-equilibrium MD (NEMD) simulations of heat transport through the z -direction of the systems, the outermost layers of both sides of the simulation domains (colored cyan) were fixed to their original positions to maintain a constant volume. Thermostats were situated at four consecutive layers (colored orange and blue) next to the outmost layers. Meanwhile, the remaining solid and fluid atoms were free to move without thermostats applied when heat transfer occurs. The temperature of the left wall was kept higher than the right to generate

thermal energy fluxes from left to right. Periodic conditions were applied in the x - and y -directions.

In this study, we used the truncated (12–6) Lennard-Jones (LJ) potential to model the interactions between atoms as follows

$$U_{\text{truncated}}(r_{ij}) = 4\varepsilon \left[\left(\left(\frac{\sigma}{r_{ij}} \right)^{12} - \left(\frac{\sigma}{r_{ij}} \right)^6 \right) - \left(\left(\frac{\sigma}{r_c} \right)^{12} - \left(\frac{\sigma}{r_c} \right)^6 \right) \right], \quad (2)$$

where ε is the depth of the potential well, r_{ij} is the intermolecular distance, σ is the finite molecular distance at which the interatomic potential is zero, and r_c is the cut-off distance of 1.0 nm. The interaction parameters and atomic properties used in this study are shown in Table 1. The interactions between the wall (or substrate) atoms are fixed as $\varepsilon_{\text{WW}} = 9\varepsilon_{\text{FF}}$ and $\sigma_{\text{WW}} = \sigma_{\text{FF}}$. The mass of the wall atoms is fixed as equal to that of fluid argon. The interaction energy between the monolayer atoms ε_{MM} is varied between $5\varepsilon_{\text{FF}}$ and $20\varepsilon_{\text{FF}}$, whereas σ_{MM} is fixed to σ_{FF} . The mass of the monolayer atom is varied between $0.5m_{\text{F}}$ and $16m_{\text{F}}$. The intermolecular interaction between the wall and fluid atoms, as well as between the monolayer and fluid atoms are kept $\varepsilon_{\text{WF}} = \varepsilon_{\text{MF}} = 0.2\varepsilon_{\text{FF}}$. Meanwhile, the interaction parameters between the wall and monolayer atoms are estimated from the Lorentz-Berthelot (L-B) mixing rules [55]. In all simulations, a cut-off distance of $3\sigma_{\text{FF}}$ is used.

The heat flux \vec{Q} in the fluid is calculated by using the Irving–Kirkwood (I–K) expression as follows [56,57]:

$$\vec{Q} = \frac{1}{\text{Vol}} \left\langle \sum_i v_i e_i - \sum_{i<j} (f_{ij} \cdot v_j) r_{ij} \right\rangle, \quad (3)$$

where e_i is the per-atom energy (including potential and kinetic energy) of atom i , v_i is the velocity of atom i , f_{ij} is the force acting on atom i from atom j . Here, the volume was defined within the fluid domain by considering the contribution of each argon molecule.

Once the heat flux is calculated, the thermal conductivity of fluid argon can be obtained from the Fourier law. Also, we compute the vibrational density of states (VDOS) of atoms at the interface using the Fourier transform of its velocity auto-correlation function (VACF) as:

$$\text{VDOS}(\omega) = \int_0^{+\infty} Z(t) e^{-i\omega t} dt, \quad (4)$$

where the VACF is defined as $Z(t) = \langle \vec{v}(t) \cdot \vec{v}(0) \rangle$. According to condensed matter physics, the VDOS of a system characterized by the number of states per interval of energy at each energy level that is available to be occupied by phonons.

Interaction	ε	σ	m
Fluid–Fluid (F–F)	ε_{FF}	σ_{FF}	m_{F}
Wall–Wall (W–W)	$9\varepsilon_{\text{FF}}$	σ_{FF}	m_{F}
Monolayer–Monolayer (M–M)	$[5\sim 20]\varepsilon_{\text{FF}}$	σ_{FF}	$[0.5\sim 16]m_{\text{F}}$
M–W	$\sqrt{\varepsilon_{\text{MM}}\varepsilon_{\text{WW}}}$	$(\sigma_{\text{MM}} + \sigma_{\text{WW}})/2$	
W–F	$0.2\varepsilon_{\text{FF}}$	σ_{FF}	
M–F	$0.2\varepsilon_{\text{FF}}$	σ_{FF}	
$\varepsilon_{\text{FF}} = 0.0103 \text{ eV}$ $\sigma_{\text{FF}} = 0.3405 \text{ nm}$ $m_{\text{F}} = 39.948 \text{ gram/mol}$			

Table 1 Interaction parameters studied in the simulation domain

Simulations start with an NVT (i.e., constant number of atoms, constant volume, and constant temperature) ensemble applied to the entire system. In this stage, the Maxwell-Boltzmann velocity distribution is used for the initial velocities of all atoms, while the Nose-Hoover thermal thermostat maintains system temperature at 100 K. Subsequently, the hot and cold reservoirs are respectively subjected to 110 K and 90 K using Langevin thermostats NVE (i.e., constant number of atoms, constant volume, and constant energy). The simulation time step is set to 1.0 fs. The simulations are performed for 12 ns: the first 3 ns to allow the systems to reach equilibrium, the next 3 ns to ensure the systems to gain a steady state in the presence of heat flux, and the last 6 ns for averaging. All simulations in this study are carried out using LAMMPS [20].

Before we present the temperature distributions and discuss the effects of the monolayer, we must demonstrate the local thermal equilibrium (LTE) in the system. It is known that the local temperature can be defined only if the LTE is established. In this paper, the temperature distributions are obtained using slab bins parallel to the walls. For instance, slab bins 0.2628 nm and 0.4 nm in thickness are used to observe the local temperatures in solid walls and fluids, respectively. Figure 1b shows the distribution of velocity components of atoms contained in one bin at different positions (i.e., in the mean position of the left solid wall, in the mean position of the fluid region, and at the mean position of the monolayer particles in the colder side when $m_M = 12m_F$ and $\epsilon_{MM} = 10\epsilon_{FF}$). The results reveal that atomic velocity components satisfy the Maxwell-Boltzmann distribution very well; thus, the LTE is established.

2.4. Results and Discussion

2.4.1 Effect of monolayer on interfacial heat transfer

To provide a general picture of the effect of monolayer coating on heat transfer at solid–fluid interfaces, we show in Figure 2.2 the temperature distributions along the z -direction of channels without and with monolayer. From Figure 2.2 (b–d), we keep the interaction energy of monolayer at $\epsilon_{MM} = 10\epsilon_{FF}$, while gradually increasing its mass. In order to determine the interfacial temperature jumps, we extrapolate the linear temperature from the fluid region to the solid surfaces, which are described by the black arrows. Throughout our analysis, surface positions are defined at the mean position of the solid surface adjacent to the fluid.

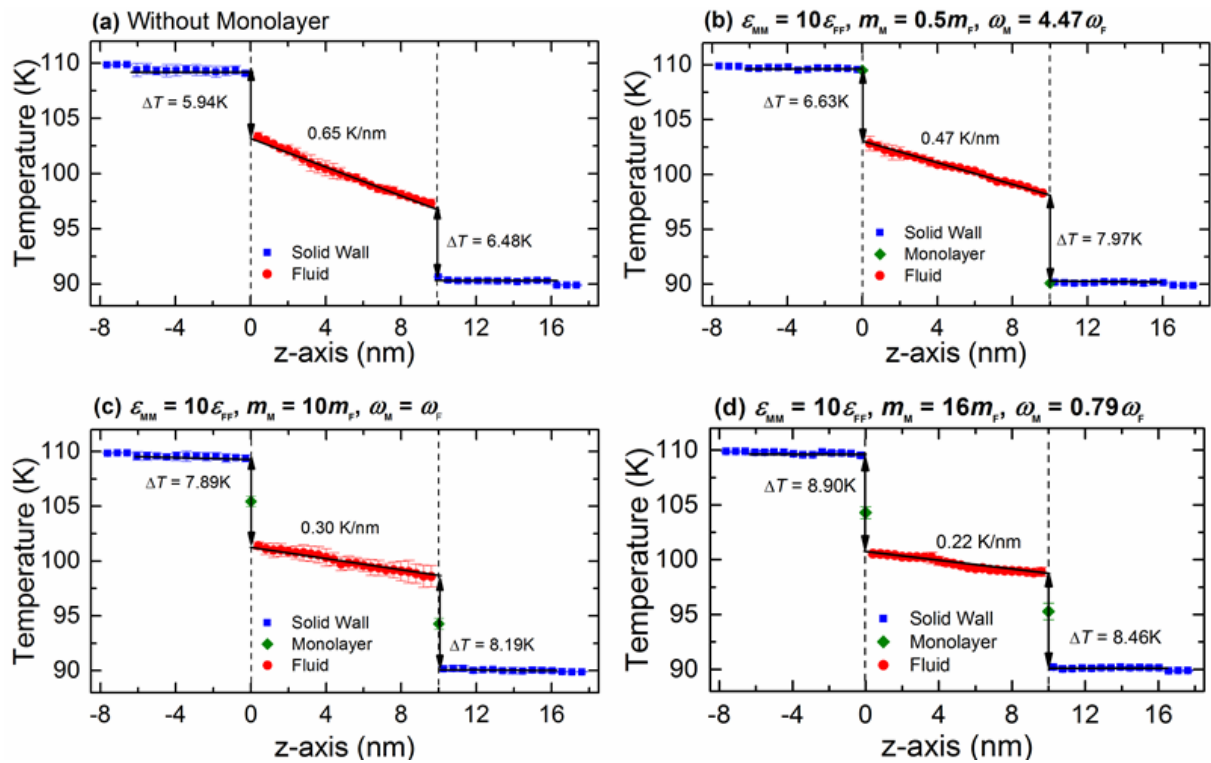


Figure 2.2. Typical temperature profiles across the wall-fluid interface (a) without and (b-d) with monolayer coated for $\epsilon_{MM} = 10\epsilon_{FF}$ at various values of m_M

When the monolayer is coated, the surface positions are then at the mean position of the monolayers. We also observe additional temperature jumps between the solid substrate and monolayer interfaces, indicating the impact of solid–solid interactions of nanocomposite structure into the overall thermal resistance at solid–fluid interface. For such a case, the temperature jumps need to be defined considering both interface (i.e., monolayer–fluid) and near-interface (wall–monolayer) temperature discontinuity. Therefore, we extrapolate the linear temperature from the wall substrate across the monolayer. The results shown in Figure 2.2 demonstrate the effects of monolayer as seen in the variation in temperature jump and temperature gradient within the fluid region compared to the substrate–fluid case. In addition, there is a slight discrepancy in temperature jumps at the hot and cold sides; however, no tendency is observed. Therefore, in the following, Kapitza length is shown as an average of the two walls.

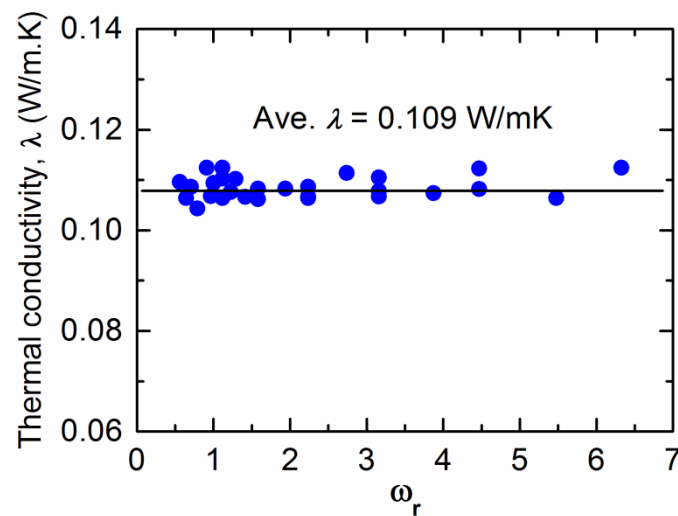


Figure 2.3. Dependence of thermal oscillation frequency between monolayer and fluid on thermal conductivity (Black line represents the value for λ without monolayer coating)

Figure 2.3 shows the thermal conductivity (λ) measured in the confined fluid. The average thermal conductivity of the bulk fluid Argon at 100K is in agreement with other MD

Studies [16,27,58] (where the relative deviation of λ is 0.9% to 7.66%), as well as in experiments [59,60] (where the relative deviation of λ is 3.2% to 4.63%). The results from Fig. 3 reveal that the thermal resistance on the interface solely depends on the interfacial characteristics, and the thermal conductivity of the fluid is independent of the thermal resistance at the interface. In this study, the effect of monolayer is studied by the variation of its atomic mass (m_M) and particle–particle interaction energy (ε_{MM}). Therefore, it is interesting to know the contribution of m_M and ε_{MM} to the interfacial heat transfer.

2.4.2 Role of monolayer mass and interaction energy

2.4.2.1 Impact on Kapitza Length

At first, we define $L_{K,r}$ as the ratio of the Kapitza length with a monolayer (L_{K-WMF}) to one without a monolayer coating (L_{K-WF}) near the wall–fluid interfacial region (i.e. , $L_{K,r} = \frac{L_{K-WMF}}{L_{K-WF}}$). Therefore, we plot the variation of Kapitza length versus monolayer mass (c.f. Figure 2.4a) and monolayer interaction energy (c.f. Figure 2.4b). Here, after reaching the minimum, $L_{K,r}$ increases monotonically with the increase of the monolayer mass independent of its interaction energy. In addition, the monolayer surface for different ε_{MM} doesn't show any significant effect on $L_{K,r}$. Hence it would seem to be the monolayer-mass that plays a dominant role in the interfacial thermal resistance, as demonstrated also in Figure 2.2.

Note that the vibrating period of monolayer particles continuously gets longer with subsequent increase of m_M regardless of any lower value for ε_{MM} . Thus, the monolayer surface continuously becomes very rough. However, the amplitude of the respective particles weakly depends on atomic mass for a high stiff surface (increased interaction energy between surface particles) that is largely controlled by the wall's temperature [5,6,61]. Primarily, $L_{K,r}$ is found to be smaller for lighter monolayer particles than heavier particles for all the cases of

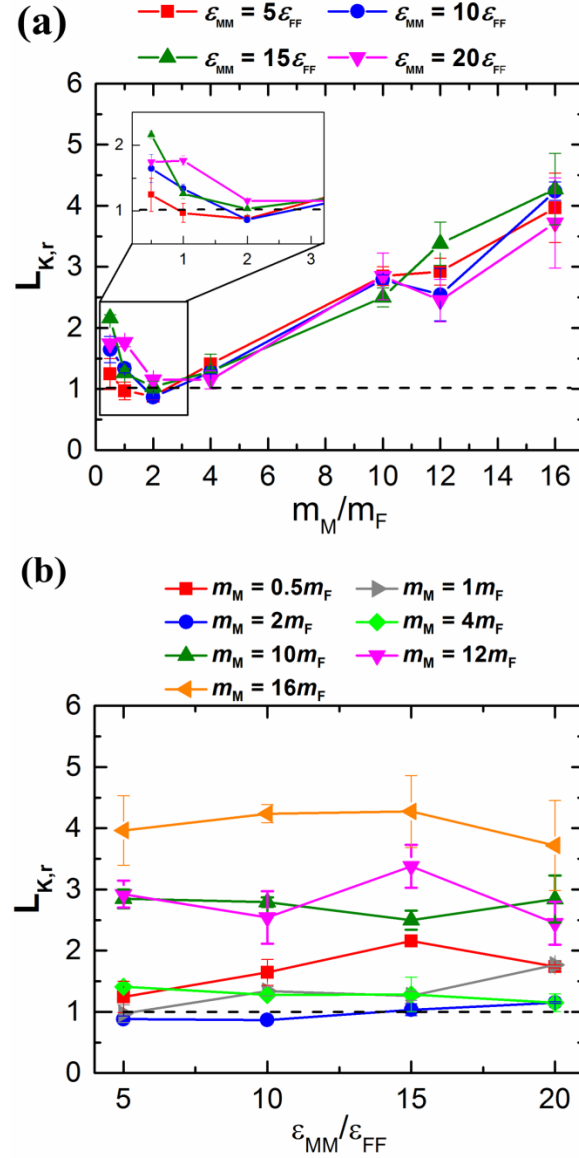


Figure 2.4. Variation of $L_{K,r}$ as a function of (a) m_M at different $\varepsilon_{MM}/\varepsilon_{FF}$ and (b) $\varepsilon_{MM}/\varepsilon_{FF}$ at different m_M

ε_{MM} (see Figure 2.4a). Starting from $m_M = 0.5m_F$, $L_{K,r}$ likely to decrease mainly due to the reduced vibrational mismatch between the absorbed fluid and the solid surface at the interfacial region. Consequently, a reduced $L_{K,r}$ is observed for a delicate amount of mass at $m_M = 2m_F$, which marginally varies for different ε_{MM} around the dashed line. This line represents the result of Kapitza length at the solid–fluid interface without monolayer coating. Afterward the interfacial region experienced a greater vibrational mismatch between the

respective materials, and eventually, the $L_{K,r}$ becomes critical for heavy monolayer particles (i.e., $m_M > 2m_F$). These results indicate that the thermal vibration of monolayer surface, which is light in weight, similarly correlated with the wall and fluid particles as the vibrating period is considerably very short. In contrary, heavier monolayer molecules further hinder the heat transport due to the increased elastic properties as well as long vibrating period at the substrate–monolayer and monolayer–fluid region in spite of any alteration of ε_{MM} . However, it is still unclear what factor mainly contributes to the $L_{K,r}$ for different values of ε_{MM} .

In Figure 2.4b, the $L_{K,r}$ fluctuates around an average value along each respective mass curve; therefore, variation in ε_{MM} contributes a minor part to further change in the $L_{K,r}$. For the case of $m_M = 2m_F$, $L_{K,r}$ is slightly under the dashed line when $\varepsilon_{MM} = 5\varepsilon_{FF}$, that has gone up to more than unity when $\varepsilon_{MM} = 20\varepsilon_{FF}$. Such an observation also has been found for almost the entire remaining strong monolayer surface ($\varepsilon_{MM} = 15\varepsilon_{FF}$ or $20\varepsilon_{FF}$). This indicates that ε_{MM} has an indirect but important effect at the interface when the substrate is coated with monolayer. In 2011, Liang and Tsai studied the effect of single atom thick film confined between two dissimilar solids [53]. They also found that the interfacial thermal resistance slightly increases with the increase of film–solid binding strength.

2.4.2.2 Impact on Density Profiles

To provide more insight into the effects of monolayer mass and monolayer interaction energy, we first explore the distribution of fluid argon near the surface as shown in Fig. 5. For all cases, fluid atoms form layered structures due to surface force penetration depth and local fluid-fluid interactions. The molecular structure of fluid at the interface is an important factor in understanding the interfacial thermal resistance. During recent decades, density peaks and depletion length (i.e., the distance between the solid surface and first peak density) have been

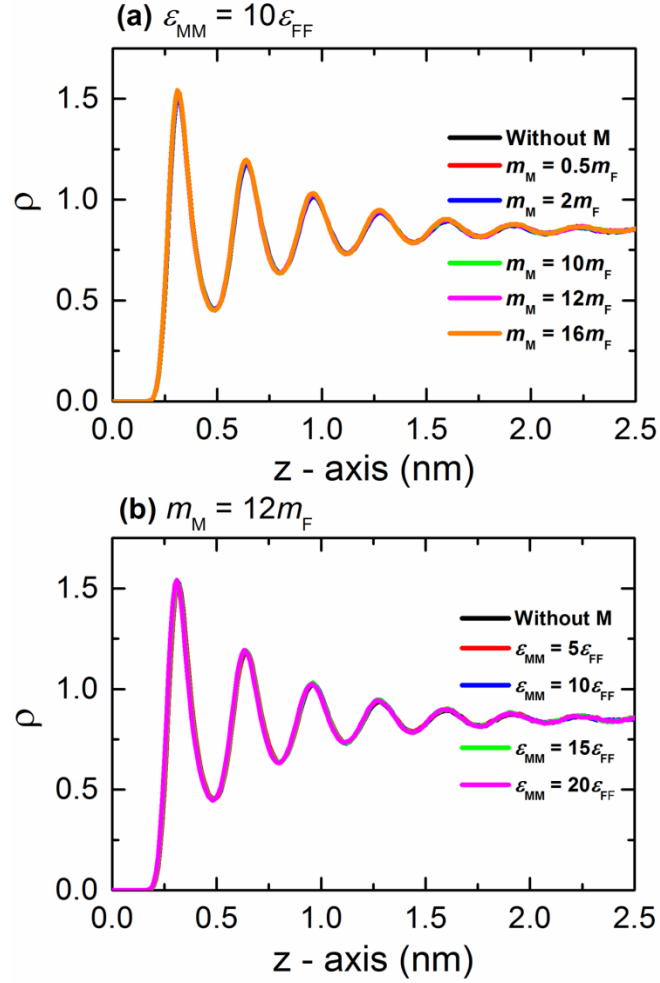


Figure 2.5. Density profiles near the hot wall for (a) $\epsilon_{MM} = 10\epsilon_{FF}$ at various values of m_M and for (b) $m_M = 12m_F$ at various values of ϵ_{FF}

two major factors for explaining the energy and momentum transport at the interface [3,11,12,37,50,62]. However, the results from Figure 2.5 show that the fluid spatial density distributions remain unchanged in spite of any change in monolayer properties. For instance, the first peak of number density near the solid surface as a function of m_M and ϵ_{MM} is 1.5317 ± 0.0097 and 1.5314 ± 0.0078 respectively for all of the cases. These observations indicate that the fluid argon was unable to change their motion after interacting with the monolayer particles. This dearth of concurrence between fluid and monolayer coated solid particles leads to the more discontinuity at the interface, which results in higher interfacial

thermal resistance. Besides, change in ε_{MM} has no impact on the interaction between monolayer and fluid particles. This tendency suggests that the thermal oscillation frequency of monolayer particles doesn't have any effect on the fluid layering near the solid-fluid interface. However, Asproulis et al. Frank et al. found that the fluid density near the surface is highly affected by the variation of wall mass and stiffness, which contrast to our results [5,6,63]. The reason is that, in their case, the elastic properties of all the wall particles were varied to quantify the oscillatory motion of fluid particles. Therefore, both the roughness and smoothness of solid surface play a dominant role on the fluid structure near the interface.

2.4.2.3 Impact on Vibrational Density of States

To comprehensively understand the influence of monolayer coating on $L_{K,F}$, we investigate the vibrational density of states, (VDOS; i.e., number of vibrational modes per unit volume and frequency), during NEMD simulation using equation 4. Particularly VDOS helps to quantify the change of phonon spectrum due to the mismatch in vibrational properties of different crystal structures in contact across an interface [64]. Besides, at nanoscale, thermal motions of fluid particles near the solid surface started to freeze, and form a layered structure at the solid-fluid interface due to the surface force and local fluid-fluid interaction. This layer also referred to as the “solid-like fluid layer” [11,37,61,62]. Therefore, we consider the first fluid layered structure near the solid surface to calculate the VDOS of fluid particles. In Figure 2.6, the overlap portion of the phonon spectrum is quite large for the interface with lighter monolayer atoms, including only the substrate-fluid interface, than heavier monolayer atoms when $\varepsilon_{MM} = 10\varepsilon_{FF}$. Basically, the overlap degree at the interface measures the degree of interfacial vibrational coupling. Increasing vibrational coupling at the interface enhances the thermal transport and thus reduces the thermal resistance. Hence, the crystal structure having $m_M = 0.5m_F$, $m_M = 2m_F$ and without monolayer interface experienced

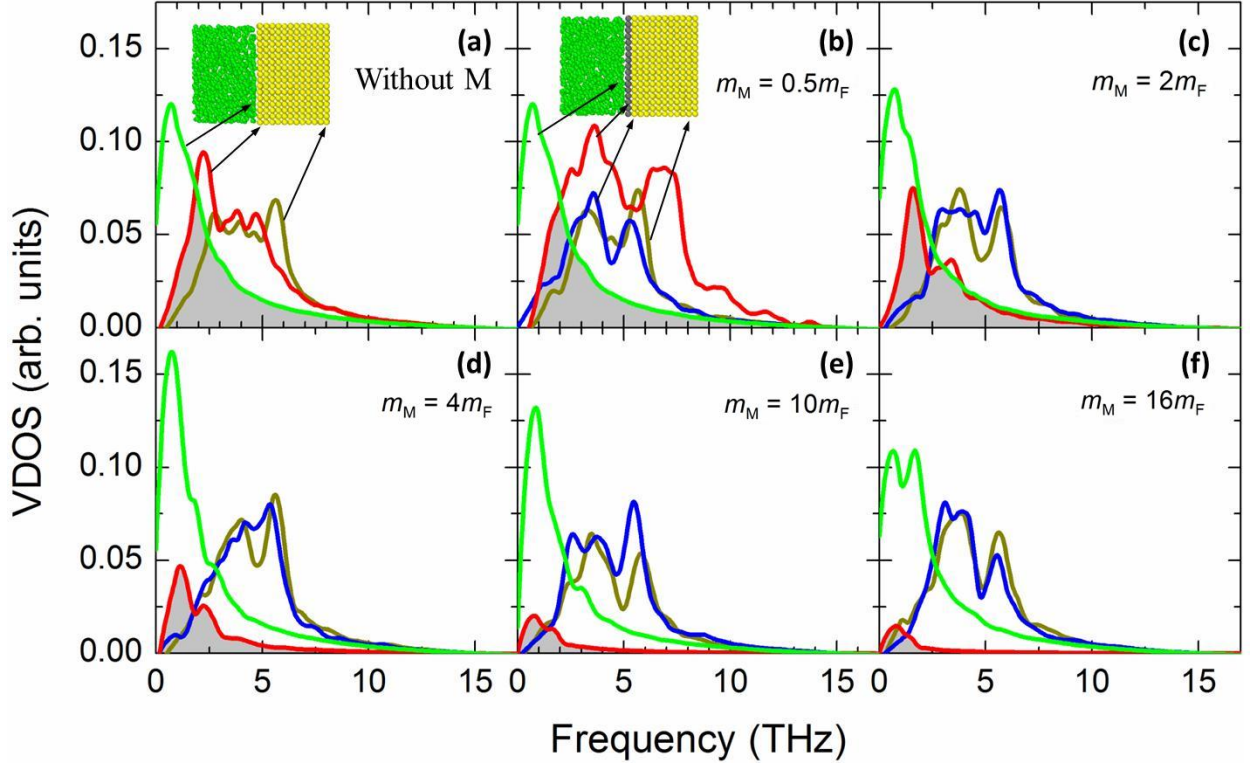


Figure 2.6. VDOS of wall, monolayer and fluid argon atoms as a function of frequency for $\epsilon_{MM} = 10\epsilon_{FF}$ at different values of m_M . **(a)** Interface without monolayer coating: surface atoms in fluid (green line), innermost substrate (red line) and bulk substrate (brown line). **(b)-(f)** Interface with monolayer coating: surface atoms in fluid (green line), monolayer (red line), innermost substrate (blue line) and bulk substrate (brown line). The grey area illustrates the overlap between VDOS

relatively much lower ITR than the interface with $m_M = 4m_F$, $m_M = 10m_F$ and $m_M = 16m_F$, which further corroborates the details in Figure 2.4. However, almost the entire phonon spectrum due to the monolayer has been used in the overlap region when $m_M = 2m_F$. In that case, peak of the phonon spectrum of the monolayer is also in good agreement with both peaks of the innermost substrate layer and the remaining bulk substrate layers, indicating a better vibrational coupling than any other cases of VDOS.

Figure 2.7 illustrates the possible scenario of the VDOS with the variation of ϵ_{MM} for $m_M = 10m_F$. Here the black line represents the innermost solid layer, and the colored lines

represent the monolayer particles. Apparently, there is no obvious change in the phonon states of the monolayer with the increase of ϵ_{MM} , and the difference in peaks between the innermost solid layer and monolayer is considerably large. This indicates that ϵ_{MM} has no such control over the thermal energy transport at the interfacial region for the heavy monolayer particles. Liang and Tsai also studied the VDOS of a thin film between two different solid materials [53]. They found better vibrational coupling at the solid–film–solid interface with the increase of film–solid binding strength. Since the solid particles oscillate about a fixed lattice point unlike fluids; therefore, increased inelastic or strong solid surface was likely to have a good agreement in the vibrations with the thin film near the interface.

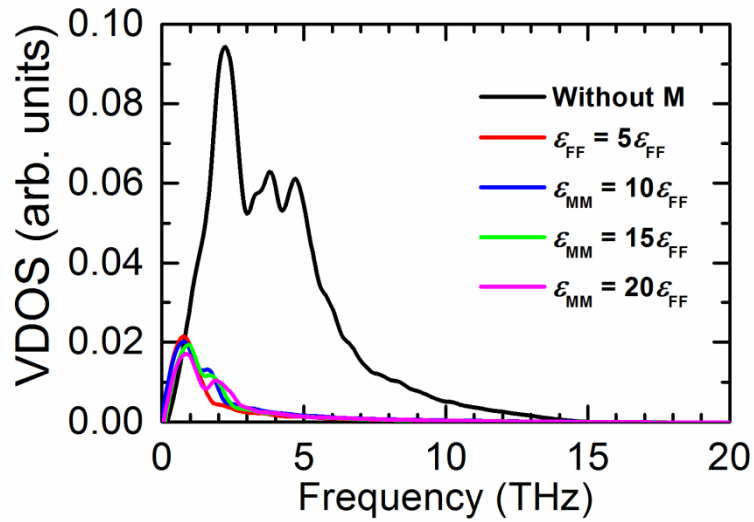


Figure 2.7. VDOS of innermost wall and monolayer atoms for $m_M = 10m_F$ at different values of ϵ_{MM}

2.4.2.4 Effect of thermal oscillation frequency on the Kapitza length

In Figure 2.8, the results of the numerical experiments are summarized to take into account the overall effects of monolayer mass and interaction energy on Kapitza length at the

interface between fluid argon and the solid substrate as a function of the thermal oscillation frequency. To quantify the behavior, we introduce a fourth-order polynomial master curve.

$$L_{K,r} = a \left(\frac{1}{\omega_r^4} - \frac{1}{\omega_r^3} + \frac{1}{\omega_r^2} - \frac{1}{\omega_r} \right) + b \quad (5)$$

in which values of the coefficients $a = 4$ and $b = 2.2$ are obtained through data fitting. For all the examined cases in the current study, $L_{K,r}$ began to decrease sharply with increasing ω_r and reached a minimum value within a very low ω_r region. Afterward $L_{K,r}$ was continuing through a marginal upward phase to finally converge to a pulsating value within the parametric range in this study.

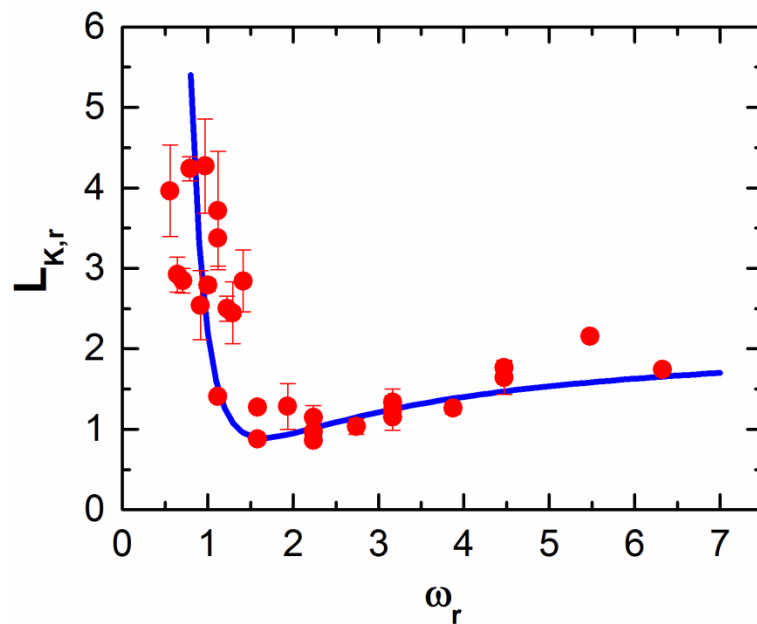


Figure 2.8. “Master” curve describing the variation of the Kapitza length at the interface between fluid argon and monolayer-coated solid substrate as a function of oscillating frequency

It is obvious that higher values of m_M will eventually be in a lower-frequency region independent of ε_{MM} . In that case, $L_{K,r}$ is found to be very high for predominantly heavier

monolayer particles. Therefore, when the monolayer surface becomes heavier, there will be a significant variation in the thermal vibration of the substrate and fluid particles that further disturbs the heat transport across the interfacial region regardless of ϵ_{MM} . This observation further justifies the details obtained from Figure 2.7. In contrast, higher values of ϵ_{MM} will surely be in the higher-frequency region and lower values of ϵ_{MM} in the lower-frequency region, regardless of a small amount of m_M . As a result, the interface experienced lower thermal resistance than the large amount of m_M . Hence, lighter monolayer molecules for any kind of ϵ_{MM} tend to be consistent with the thermal vibration between substrate and fluid particles, which helps to minimize the deficit of heat transport across the interfacial region. Despite having a better vibrational coupling for lighter m_M , after reaching a minimum value, $L_{K,r}$ increases gradually with increasing ω_r as well as ϵ_{MM} . This indicates that the strong monolayer surface created more $L_{K,r}$ than a flexible monolayer surface for lighter monolayer particles. Hence, ϵ_{MM} act as a deciding factor for the interfacial thermal resistance when the m_M is likely to have a low weight. In 2008, Kim et al. also suggest that Kapitza length increases with the increase of thermal oscillation frequency, which is in accordance with the lighter monolayer particles [16]. Therefore, a minimum is appeared in the master curve to signify the effect of m_M and ϵ_{MM} as a function of thermal oscillation frequency.

2.5 Conclusions

The role of monolayer particles mass (m_M) and interaction energy (ϵ_{MM}) on Kapitza length between the monolayer coated solid surface and fluid argon has been extensively analyzed through non-equilibrium molecular dynamics simulation. Within this monoatomic nano-composite structure, thermal conductivity of fluid showed a constant value at 100 K using Fourier's law. The fluid density structure near the solid surface is also independent of any change in m_M and ϵ_{MM} . This indicates that heat transport at the interfacial region solely depends on the monolayer properties. Considering the mutual combination of m_M and ϵ_{MM} ,

we also observed that the temperature jump increases with decreasing ω_r , suggesting a greater interfacial mismatch between the particles with a lower oscillation frequency.

Primarily, our results indicate that m_M is the dominant factor for controlling the amount of heat transport at the interface as the Kapitza length monotonically increases with increasing m_M , regardless of ϵ_{MM} . Because the vibrational mismatch of atoms continuously increases with the subsequent addition of mass, the measured $L_{K,r}$ was expectedly much higher for heavier monolayer particles than lighter monolayer particles for a given value of ϵ_{MM} . This is because the interaction energy between heavier monolayer particles has no control over the interfacial thermal resistance which results in a greater vibrational mismatch between the materials near the interface. On the other hand, for lighter monolayer particles, the interaction energy of monolayers is likely to maintain a better vibrational coupling with the solid substrate. Therefore, even if the vibrational mismatch marginally increases with the increase of m_M , ϵ_{MM} minimizes that mismatch which eventually leads to a reduced Kapitza resistance at the interfacial region.

Further improvement of interfacial thermal transport is possible when the nanocomposite materials remain mismatched in the lattice structure. Hence, further examinations of the lattice mismatch monolayer surface with the existing monatomic crystal structure will be a part of our future research.

CHAPTER 3

Nanopore Flow Modeling for the Transportation of Argon through Nanoporous Graphene Membrane

3.1. *Abstract*

Pressure driven transport mechanism of liquid argon through nanoporous graphene membrane has been analyzed using non-equilibrium molecular dynamics simulation. In this study, we investigate liquid dynamics properties such as local density, pressure variation, and viscosity depending on the flow region. With the movement of specular reflection wall (SRW) at the end of front and back reservoir, pressure difference takes place mainly due to the change in relative distance between the argon molecules in the corresponding reservoir. The interfacial pressure difference strongly depends on the intermolecular force of graphene membrane governed by the layered structure of liquid and the applied flow velocity. The local viscosity was calculated from the nano-channel of argon sheared by graphene walls. The argon velocity adjacent to the pore edge was considered as slip velocity, which provides an update in the Sampson flow equation. We observed that the entrance interfacial pressure and higher local viscosity in the vicinity of graphene membrane associated with the optimized definition of wall/fluid boundary near the pore edge play a critical role for the permeation of argon through NPGM.

3.2. *Introduction*

Nanoporous membranes (NPM) can be made from a wide range of materials including novel polymers [65], zeolites [66], metal-organic framework [67], carbon nanostructures[68], etc. The pore size in these NPM structures can be varied from

subnanometer to a few nanometers. Therefore, owing to their small length scales and large surface-to-volume ratio, the liquid molecules exhibit inhomogeneous configurations, properties, and energetics near the solid/liquid interface from those of their bulk counterparts, while transporting through the NPMs. These unique interfacial characteristics play a key role in understanding the mass and energy transport in confining nanoenvironments. Recent experimental and simulation studies have shown fast transport of water through carbon nanotubes (CNT) membranes. For example, Holt et al.[69] and Majumder et al.[70] experimentally found that the permeation rate of water in CNT, with pore diameter 2 to 7 nm, can be more than 3 to 5 orders of magnitude faster than the continuum prediction. Using molecular dynamics (MD) simulations, Hummer et al.[71] and Skoulidas et al.[72] also shown that the water or gas molecules inside CNT permeate much faster than the prediction of continuum hydrodynamics. This enhanced transport rate inside CNT suggests the effects of nanochannel size on intrinsic liquid properties, such as density, shear stress, viscosity, etc, which is yet to be fully characterized at nanoscale.

The main advantages of NPMs are low energy consumption, allow flow of desired molecules and reject undesired molecules, and exhibit robustness during operation. In this regard, graphene is definitely a noble material considering its remarkable mechanical strength, electrical, thermal and optical properties [73–76]. This single atom thick 2D material has sp²-hybridized carbon atoms positioned in a honeycomb-like (hexagonal) lattice structure[77]. The van der Waals (vdW) thickness of graphene layer is ~0.34 nm making it the thinnest known material. It also offers partially transparent to vdW's and electrostatic interactions which further improve the wettability between two different materials placed on either side of graphene [78,48,79]. Besides sub-nanometer pore in graphene can be generated by ion bombardment followed by chemical etching[80] etc. This single layer or a few-layer porous graphene membrane can be tailored to sieve ions efficiently from seawater for

desalination[81], differentiate between polar and nonpolar liquids for flow sensors[82], and enhance proton transport in fuel cell applications[83–85].

Numerous theoretical studies using molecular dynamics (MD) simulation have been focused on the transport of water and ions through nanoporous graphene membrane (NPGM) driven by pressure [86–90] and electric fields [91–93]. Based on these researches, high permeance and high selectivity of certain groups of molecules greatly influenced by the pore size, pore functionalization and applied external force. For instance, Suk et al. reported that for smaller pore diameters, where single-file water structure is observed, water flux is lower in NPGM than CNT mainly due to the interruption in hydrogen bonding and structuring of water molecules in graphene nanopores [89]. However, pore diameter larger than 0.8 nm, water flux was found to be higher in NPGM than CNT indicating reduced energy barrier at the pore entrance. It was also reported that, by bonding hydroxyl or carboxylic groups ($-\text{OH}$ or $-\text{COOH}$) to the edges of graphene pore, the water flux further increases while rejecting salt ions [86,88]. Since the effective diameter of salt ions (Na^+ and Cl^-) increases as a result of the hydration effect, the ions encounter large energy barriers in the pore diameter smaller than ~ 0.7 nm. This type of ion blocking, where the pore diameter is smaller than the hydrated diameter of the ions, is often termed as steric exclusion. Moreover, charged or partially charged functional groups along the pore edge can lower the energy barrier for ions of opposite charge leading to the cation/anion selectivity. For example, Sint et al. demonstrated that nanopore of 0.5 nm in diameter could be made cation-selective by decorating the pore with electronegative fluorine or nitrogen atoms [91]. Zhao et al. also observed that the presence of negative charge at the edge of graphene pore with 0.4 nm and 0.8 nm diameter can remarkably impede the passage of Cl^- while enhancing the transport of K^+ [93]. Similar observation about ionic selectivity also been found experimentally in monolayer graphene membranes demonstrated by O'Hern et al [80]. In addition, about 93% rejection of salt ions

with much less application of pressure is possible in negatively charged graphene pore (with 0.99 nm diameter) than that in pristine graphene membrane case, reported by Nguyen et al. [94,95]. Therefore, the ion selectivity greatly dependent on the pore size and the charges on the pore edge.

The liquid dynamics properties predominantly control the mechanism of mass transport and ionic selectivity in NPMs. At the macroscale, numerous studies on the topic of permeation through porous structure have been performed [96–99]. In these researches, incompressibility of the flow and no-slip boundary condition was assumed in the continuum model. However, at nanoscale, the intermolecular force of the nanostructure becomes dominant mainly due to the size of the wall molecules, which is very close to the characteristics physical scaling length of the nanoconfined liquid molecules, and the interaction between wall–fluid molecules at the solid/fluid interface. Consequently, this creates slip effect [34,100,101] and Kapitza length [1,3,102] at the solid/ fluid interface. Moreover, the liquid molecules form a solid-like layering structure over several atomic distances from the solid wall which is observed by both experimentally [14,15] and numerically [37,61,62]. The dynamics of this liquid layered structure also produce a different shear rate and viscosity at the wall/fluid boundary than the bulk flow region [17,18,34]. In addition, the effective viscosity of nanoconfined liquids also shows strong dependency on flow velocity[103]. These decisive effects of the molecular structure of the solid wall and liquid molecules, as well as their interactions, play a critical role in nanoscale fluid dynamics. As a consequence, the traditional continuum models fail to provide accurate predictions of flow behaviors along the nano-channels [10,19,90]. Therefore it is necessary to investigate the validity and limitations of the continuum assumptions for nanoscale liquid transport.

In addition to that, the accurate prediction of flow measurement also depends on the definition of the location of wall/fluid boundary. Previously, the location of wall/liquid boundary in nanochannel was considered at the atomic-center to center distance between the innermost solid layers[3,11,37,50], and the first peak density position of the layered structure of liquids adjacent to the solid surface[104,105,41]. At nanoscale interface, the wall/fluid boundary largely depends on the interatomic force penetration depth and the discrete nature of liquid molecules. Therefore, small changes in the wall/fluid boundary definition may cause significant deviation in the calculation of flow enhancement [106]. Thus, in molecular level fluidic transport, proper definition of the pore diameter is also necessary.

In this paper, a pressure-driven flow of simple liquid through nanoporous graphene membrane has been studied using non-equilibrium molecular dynamics (NEMD) simulations. First, two impermeable flat walls were placed at the end of front and back side of the simulation domain. Then the two walls were moved at a constant velocity in the same directions to create pressure effect. Thus a pressure difference was developed between the front and back side that pushed the argon molecules through the pore of graphene membranes. In general, simple liquid can be best described with Lennard–Jones (LJ) models that have strong correlation between virial and potential energy in their constant-volume thermal-equilibrium fluctuations (NVT ensemble) [107]. Even a complex liquid like water, in which the coulombic term is added with the LJ potential, is expected to approach simple behavior under sufficiently high pressure [108]. Therefore, in this study, the structure and dynamics of molecular model of LJ type liquid have been analyzed to reduce the computational cost. To check the limitations of the continuum assumptions, first, we characterize the liquid argon properties with respect to their interfacial and bulk flow region. Then the Sampson flow equation, proposed by Jensen and Stone et al. [109], was modified based on the slip velocity adjacent to the edge of graphene nanopore. We also calculate local

viscosity of argon based on the shear driven flow simulations. Finally, the effect of pressure, viscosity and pore boundary was investigated based on the characterized fluid dynamics properties by utilizing the slip modified continuum flow equation. We observed that interfacial pressure near pore entrance, flow velocity, and local viscosity near the solid surface strongly connected with the optimized definition of wall/fluid boundary play a critical role for the accurate flow prediction inside graphene nanopore.

3.3. Theoretical background:

In this present study, the Reynolds number of liquid argon is in the range of (0.01~0.1). For such low Reynolds number flow behavior, Sampson solved the Stokes flow through a circular pore in an infinitely thin wall in the creeping flow regime for a Newtonian liquid [96]. The boundary conditions are that (i) incompressibility of the flow throughout the system, (ii) the velocity decays uniformly, (iii) the no-slip condition everywhere in the thin wall, and (iv) the pressure reaches two different constants at $+\infty$ and at $-\infty$. Due to the symmetry of the geometry, the pressure difference ($\Delta P = P_{-\infty} - P_{+\infty}$) from an infinitely thin wall is therefore given by,

$$\frac{\Delta P}{q} = \frac{3\mu}{a^3} \quad (1)$$

where, q is the volumetric flow rate, μ is the viscosity of the liquid, and a is the pore radius. In order to find an approximation for the velocity profile in pore, Sampson introduced a stream function (ψ) in spheroidal coordinate (ξ, η, θ) . These coordinates are obtained from the cylindrical coordinates (r, z, θ) by the transformation,

$$z + ir = a \sinh(\xi + i\eta) \quad (2)$$

with $a > 0, 0 \leq \xi < \infty, 0 \leq \eta \leq \pi$ and $0 \leq \theta < 2\pi$. Then Sampson showed that (ψ) for flow through a circular pore in a plane wall is given by,

$$\psi = -\frac{q}{2\pi} (1 - \cos^3 \eta) \quad (3)$$

Then, the flow profile inside pore can be computed directly from Sampson's stream function in cylindrical coordinates as:

$$v_{z,a} = \frac{a\Delta P}{2\pi\mu} \sqrt{1 - \left(\frac{r}{a}\right)^2} \quad (4)$$

At the nanometer scale, it has been noted that the interactions between wall-liquid molecules are substantially different from classical liquid transport. This is due to the intermolecular forces of wall molecules, thermal/velocity slip, the discreteness of liquid molecules adjacent to the solid surface, and the local viscosity at the solid/liquid interface[19]. Thus, in case of the mobility of argon molecules through NPGM, it is expected that the flow exhibits a slip tendency inside graphene nanopore which further modify the Sampson equation given by,

$$v_{z,a} = \frac{a\Delta P}{2\pi\mu} \sqrt{1 - \left(\frac{r}{a}\right)^2} + u_s \quad (5)$$

Therefore, it is necessary to investigate the effect of interfacial entrance and exit pressure, and local viscosity in the vicinity of graphene membrane correlated with optimized definition of wall/liquid boundary near the pore edge for the prediction of argon velocity profile.

3.4. Molecular dynamics simulations:

Figure 3.1 shows the simulation domain consisting of liquid argon transporting from front reservoir to back reservoir through a pore of graphene membrane. The model of NPGM

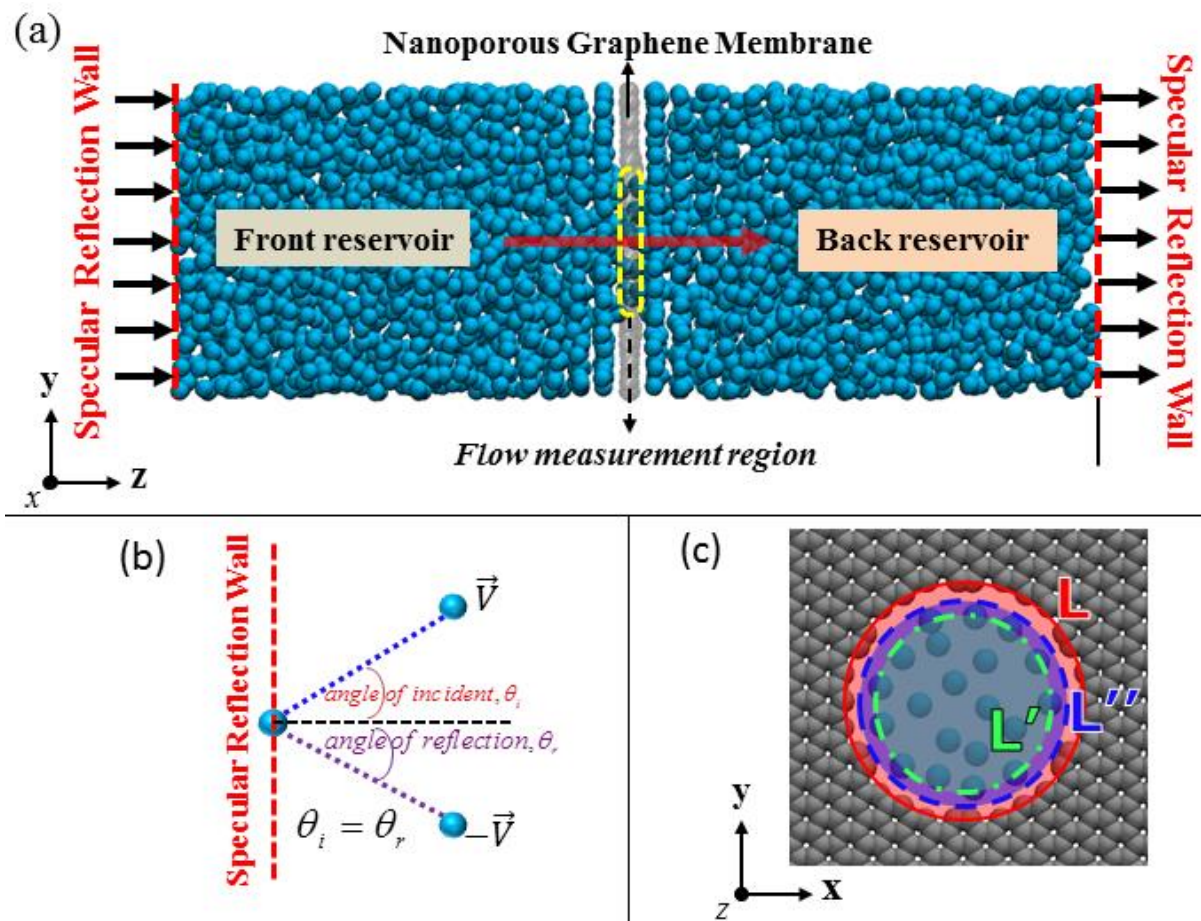


Figure 3.1. (a) Schematics of the flow of liquid argon through nanoporous graphene membrane, (b) Physical description of specular reflection wall, and (c) Insight of graphene pore with three probable pore boundary

(3.69 nm × 3.6927 nm) was placed at the center ($z = 0$) of the simulation box parallel to the xy -plane. A circular pore was generated by removing the carbon atoms at the center of graphene membrane. Initially, the pore radius was approximated as $a_{cc} = 1.10925$ nm corresponds to the pore center to atomic center of carbon atoms in the pore edge. Periodic boundary conditions were applied in both x -axis and y -axis direction of the simulation domain. Two specular reflection walls (SPW) was placed at the end of front and back reservoir along the xy -plane. When the liquid argon attempts to move through the wall, this flat wall acts as a specular mirror to reflect the particles by reversing the corresponding

component of argon velocity. In that case, the angle of incident and the angle of reflected argon atom remain same as shown in figure 1b. Therefore, the liquid dynamics properties of argon molecules in the bulk flow region become independent after colliding with the specular wall. The distance between each SRW and graphene membrane was initially set at 6 nm in the direction of z axis.

Interatomic interactions between the argon molecules were calculated using truncated Lennard-Jones (LJ) (12-6) potentials given by:

$$V_{truncated}(r_{ij}) = 4\varepsilon \left[\left(\left(\frac{\sigma}{r_{ij}} \right)^{12} - \left(\frac{\sigma}{r_{ij}} \right)^6 \right) - \left(\left(\frac{\sigma}{r_c} \right)^{12} - \left(\frac{\sigma}{r_c} \right)^6 \right) \right] \quad (6)$$

where, ε is the depth of potential well, r_{ij} is the intermolecular distance, σ is the finite molecular distance at which the interatomic potential is zero, and r_c is the cutoff distance. In this study, we truncated intermolecular forces at a distance of $r_c = 1.0$ nm, which is approximately equal to 3σ . The adaptive intermolecular reactive empirical bond order (AIREBO) potential was employed to model the interatomic interactions between carbon atoms in the graphene membrane. Meanwhile, the interaction parameters between carbon and argon molecules are estimated from the Lorentz-Brethelot (L-B) mixing rules[55]. The interaction parameters used in this study are shown in Table 3.1.

Interaction	ε (eV)	σ (nm)
Ar-Ar	0.0103	0.3405
C-Ar	0.005	0.303

Table 3.1. Details of the interaction parameters utilized in this study

In each reservoir, a total of 1740 argon molecules were placed. Maxwell-Boltzmann velocity distribution at 100 K was used for assigning the initial condition of all argon molecules. Then the Noose-Hoover thermostat maintained the system temperature at 100 K with two subsequent NVT ensembles (constant number of molecules, volume, and temperature). In first NVT ensemble, the initial state was equilibrated for 10 ns with timestep of 1 femtosecond (fs) to establish the equilibrium MD simulations. Finally, in second NVT ensemble, the flow was induced across the simulation domain by moving both the SRW at constant velocity (U_W) along the z -axis, while the carbon atoms of graphene membrane were vibrating about a fixed lattice point. Besides, the location of NPGM was remained static (at $z = 0$) throughout the entire simulation by fixing the 4 corner carbon atoms at their initial position. The simulation was conducted for 1 to 5 ns depending on the velocity of SRW. All the simulations were performed in LAMMPS[20].

The pressure of the liquid argon was calculated by computing the three orthogonal stresses to the x -, y - and z - directions across the simulation domain (S_{xx} , S_{yy} and S_{zz}) from the Irving-Kirkwood expression [59,60]. In our simulations, the instantaneous pressure tensor for an N particle system is calculated by the following formula:

$$S_{\alpha\beta} = \frac{1}{Vol} \left\langle m^i (v_\alpha^i - u_\alpha)(v_\beta^i - u_\beta) + \frac{1}{2} \sum_{i,j}^N (r_\alpha^j - r_\alpha^i) f_\beta^{i,j} \right\rangle \quad (7)$$

where the first term on the right-hand side is the kinetic component and the second term is the virial component. In the kinetic part, m is the mass of atom i , v is the velocity of atom i and u is the streaming velocity in the α and β directions of the cartesian coordinate system. In the virial part, $(r_\alpha^j - r_\alpha^i)$ is the relative distance vector between the atoms i and j , and $f_\beta^{i,j}$ is the intermolecular force acting on atom i by atom j .

3.5. Results & Discussion

3.5.1 Characterization of fluid dynamics properties based on respective flow region

3.5.1.1 Density distributions of liquid argon in the vicinity of porous membrane

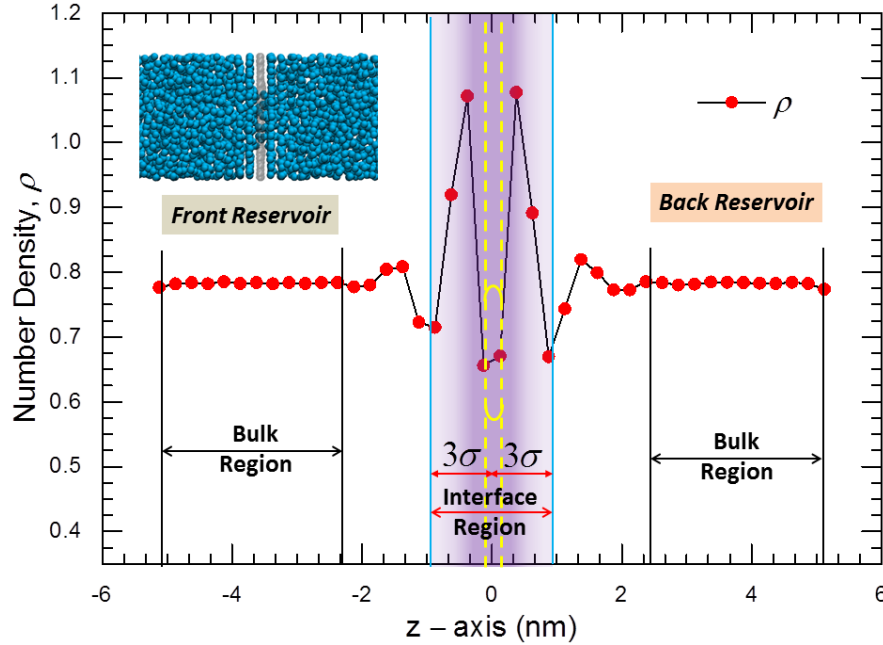


Figure 3.2. Density distribution of argon along with the axial direction of flow within $a_{cc} = 1.10925$ nm pore radius

In molecular-fluidic transport, the properties of liquid are strongly related to the molecular structure and intermolecular force of liquid near the solid/liquid interface. Hence, the density distribution of liquid argon along the axial direction in a graphene nanopore was observed as shown in figure 3.2. The simulation domain was divided into several slab bins with bin thickness $\Delta z = 0.25$ nm along the axial direction of flow to calculate the number density $\rho = \frac{N\sigma^3}{V}$ of liquid argon. The obtained values were averaged for 1 nanosecond (ns) during the equilibrium condition. Liquid argon forms oscillations with enhanced density near the NPGM and gradually converges to the constant value of approximately 0.8 in the bulk flow region of both the reservoirs. This oscillation is observed mainly due to the interaction

between carbon-argon molecules in the vicinity of graphene membrane. Although the interaction strength of C–Ar is very weak, the intermolecular force of carbon molecules is strong enough to create layered density structure of liquid at a distance 3σ from the NPGM. The oscillation near the interface region is commonly known as fluid layering[14,15,37,61,62]. However, still a portion of fluid layering is observed beyond 3σ mainly due to the smaller bin thickness of 0.25 nm, which is less than one molecular diameter. To distinctly enable the molecular distribution along the channel, the bin thickness must be ten times smaller than the molecular diameter. This bin is not appropriate for continuum analysis but provides insight into the molecular structure in a similar manner to the radial distribution function. In case of the continuum transport theories, this layered structure of fluid near the solid surface is not considered; however, their effect in nanoscale fluidic transport is significant. Because of the size effects, the liquid molecules can be absorbed by the wall molecules causing a higher density, pressure, and viscosity near the interface than other flow regions. Therefore, an investigation of the variations of argon properties over the different liquid regions (interface, boundary and flow regions) is essential for understanding nano-scale fluid flow behavior.

3.5.1.2 Pressure distributions of liquid argon in the vicinity of porous membrane

With the movement of SRW, a pressure difference between front and back reservoir started to develop in the system which mainly contributes to the mobility of argon molecules through nanopore as shown in figure 3.3a. The average of the three orthogonal normal stress components from the IK expression was utilized to calculate pressure as, $P = \frac{S_{xx} + S_{yy} + S_{zz}}{3}$.

To measure the local normal stress tensor distribution the simulation domain was divided into

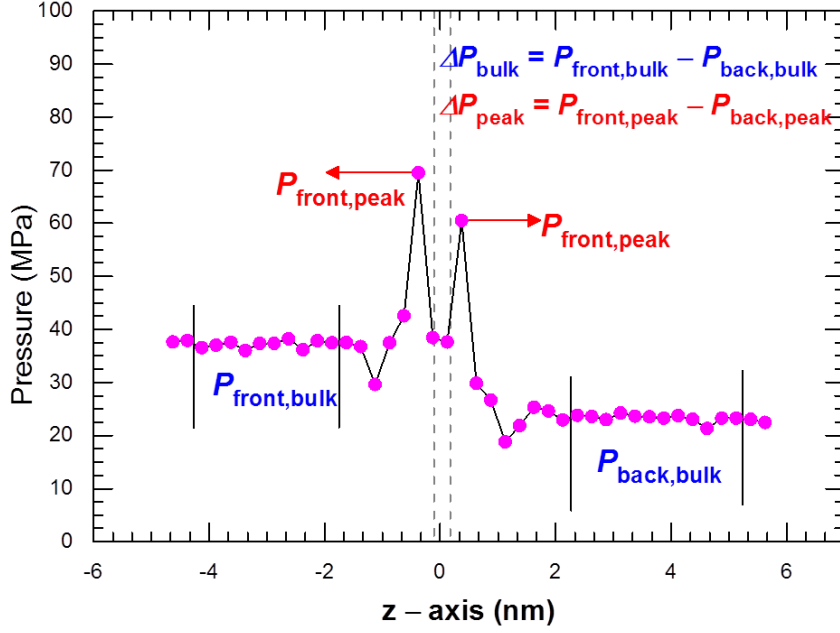


Figure 3.3. Pressure distribution of argon along the axial direction of flow within $a_{cc} = 1.10925$ nm pore radius at $U_w = 1.5$ m/sec

several slab bin along the axial direction, each of which has a volume $V_{bin} = L_x L_y \Delta z$, where $\Delta z = 0.25$ nm is the width of each bin. The data were averaged for every 0.4 ns when the movement of SRW is in the range of 0.5 to 3.5 nm from its initial position because the variation of pressure is small in this regime. After this range, rapid changes in the averaged data were observed and there was lack of enough volume to predict the bulk pressure of liquid argon in the FR. When the SRW move at constant velocity, in the bulk region of the simulation domain, the number of molecules in each slab bin of the FR increases about 2.6% and same amount of molecules decreases in each slab bin of the BR. Therefore, the local bulk density slightly increases and decreases in the front and back reservoir respectively. Meanwhile, the number of molecules in the interfacial region remains unchanged from their initial equilibrium configuration. However, the pressure difference between the corresponding liquid flow region is significant. To analyze the pressure difference, we

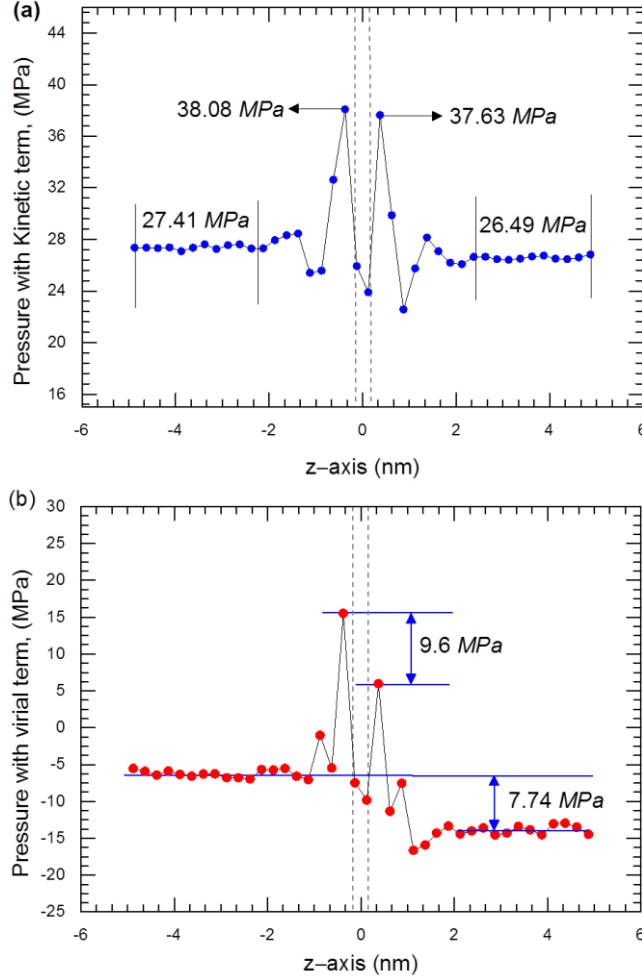


Figure 3.4. Pressure distribution with, (a) kinetic term and (b) virial term, along z axis within $a_{CC} = 1.10925$ nm pore radius at $U_w = 1.5$ m/sec

separately calculate the normal stress components for kinetic and virial term from the IK equation as shown in figure 3.4. From the kinetic term, the pressure in the bulk region was 27.41 MPa (FR) and 26.49 MPa (BR) respectively, and in the interface region was 38.08 MPa (FR) and 37.63 MPa (BR) respectively in case of $U_w = 1.5$ m/sec. This further justifies that the molecular distribution of liquid argon in the corresponding liquid flow region does not change with the established pressure difference. In contrary, from the virial term, a pressure difference was observed for $\Delta P_{bulk} = 7.74$ MPa and $\Delta P_{peak} = 9.6$ MPa. It is important to emphasize that the virial term is the result of internal contribution from intermolecular

forces between atoms across the surface. In this case, with the movement of SRW, the relative distance vector between the argon molecules across the surface decreases in the FR and increases in the BR, while the intermolecular force between the argon molecules remains unchanged from their initial equilibrium configuration. Consequently, this has a major impact on the pressure difference across the simulation domain even if the movement of SRW is very small. Therefore, pressure difference takes place mainly due to the change in relative distance between the argon molecules in the corresponding reservoir.

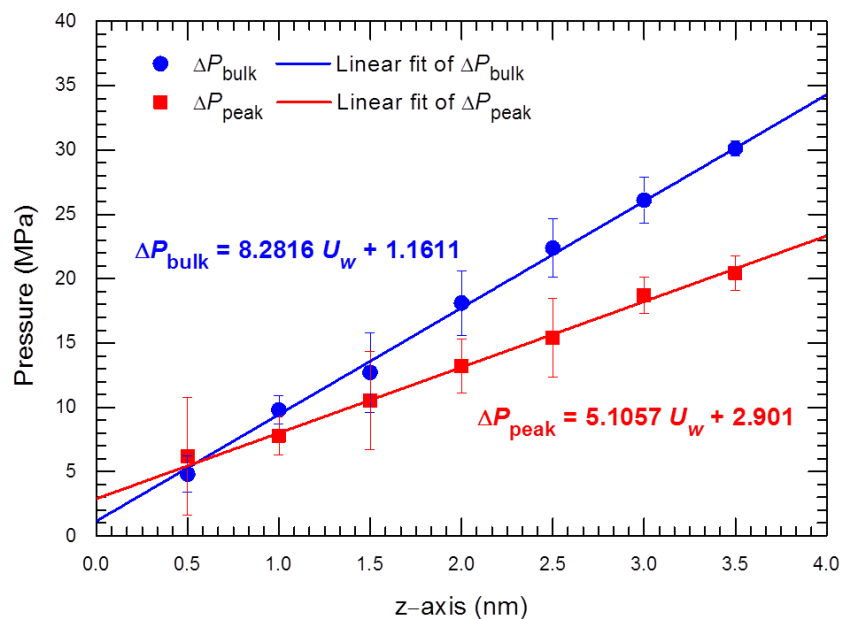


Figure 3.5. Variation of pressure difference between front and back reservoirs in the bulk and interface region respectively with the increase of U_w

It is apparent from figure 3.3 that argon pressure near the solid/liquid interface differs significantly from the bulk value. This is because of the layered structure of liquid argon due to the interaction between carbon-argon molecules in the interfacial region. Moreover, argon molecules need to overcome higher free energy-barrier during the entry into the graphene nanopore, since the peak pressure in the FR ($P_{\text{front,peak}}$) is maximum. In contrary, during exit, the peak pressure in the BR ($P_{\text{back,peak}}$) gets lower than the $P_{\text{front,peak}}$, indicating the dissipation

of energy which facilitates the motion of confined argon in the nanopore. The pressure difference between both the reservoirs at the bulk and interfacial region was considered as bulk pressure difference ($\Delta P_{bulk} = \Delta P_{front,bulk} - \Delta P_{back,bulk}$) and interface pressure difference ($\Delta P_{peak} = \Delta P_{front,peak} - \Delta P_{back,peak}$) respectively. The pressure difference linearly increases with the increase of U_w as shown in figure-3.5, while the slope of ΔP_{bulk} is much higher than ΔP_{peak} . This is because the $P_{front,peak}$ (entrance interfacial pressure) increases with the increase of U_w meaning that the entry of argon into the nanopore is becoming energetically unfavorable. Therefore, the shear stress between argon and carbon molecules at the front interface region further increases for increased flow velocity, which plays a critical role for the permeation rate of argon through NPGM. However, the $P_{back,peak}$ (exit interfacial pressure) remains unchanged regardless of any flow velocity, which suggests that the $P_{back,peak}$ only marginally contribute to the free energy barrier. On the other hand, the pressure in the bulk flow region significantly affected both the reservoir with the increase of flow velocity. Based on the results, ΔP_{peak} strongly depends on the intermolecular force of membrane governed by the layered structure of liquid and the applied flow velocity. It is also apparent that the linear fit of bulk and peak pressure difference intersect when the U_w at approximately 0.5 m/sec. Before this intersecting point, the argon velocity profile was found in disarray due to the lack of enough pressure in the system. Therefore, velocity profile started to develop inside graphene nanopore until the bulk and peak pressure difference reaches an equivalent value.

3.5.1.3 Effect of nanoconfinement on local viscosity

To calculate the local viscosity, we conducted shear driven flow simulation on liquid argon confined by graphene walls as shown in figure 3.6a. In that case, 1200 argon molecules

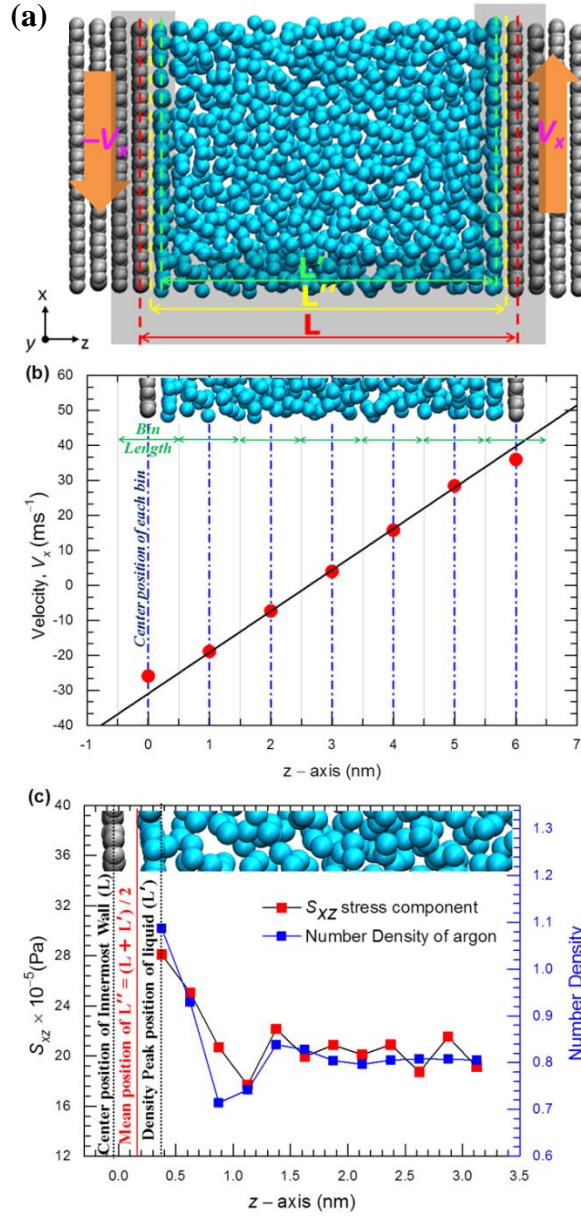


Figure 3.6. (a) Schematics of MD simulation of liquid argon sheared by graphene walls, (b) Velocity distribution of liquid argon along the z- direction of the channel, and (c) Shear stress component (S_{xz}) of liquid argon compared with density distribution from nanopore flow simulation

were simulated in a three dimensional channel with $L_x \times L_y = 4.218\text{nm} \times 22.4\text{nm}$ and $L_z = 6.0\text{nm}$ from innermost to innermost distance between the graphene walls. The wall velocity was set to $V_x = 100$ m/sec. The system configuration was maintained similar to the

nanopore flow simulation. Figure 3.6b shows the velocity distribution of liquid argon using several slab bins with thickness of 1 nm across the channel. Argon molecules velocity in the vicinity of moving graphene walls slightly deviated from the linear fitting of the mid-flow region. This suggests that the intermolecular force of the graphene walls still resist the flows even if for very weak interactions between carbon-argon molecules. Then using the equ1, the stress tensor (S_{xz}) of liquid argon parallel to the graphene wall was computed by dividing the channel into several slab bins with thickness of $\Delta z = 0.25$ nm as, $S_{xz}^{bin} = \frac{(S_{xz} N_{bin})}{L_x \times L_y \times \Delta z}$, where,

N_{bin} is the total number of argon molecules in each slab bin. Similar tendency was observed between the density distribution of argon near NPGM and stress tensor (S_{xz}) distribution of shear driven flow as shown in figure 3.6c. The shear stress component was found to be higher near the interface region referring to the dynamic structure of liquid argon.

The shear rate was obtained from the slope of two successive velocity data as shown in figure 3.7a. It is evident that the shear rate exhibits a non-uniform tendency at the solid/fluid interface than the bulk flow region. Then the local viscosity was calculated as, $\eta = -\frac{S_{xz}}{\gamma}$, where $\langle S_{xz} \rangle$ is the averaged shear component of the stress tensor within each slab bin thickness of 1 nm and γ is the applied shear rate in the same slab bin as shown in figure 3.7b. This method is proposed by Kim et al [52]. The bulk viscosity of about 1.78×10^{-4} Pa.sec also shows good consistency with the experimental results [110] under exact thermodynamic conditions. However, higher viscosity of 3.21×10^{-4} Pa.sec was found at the solid/fluid interface as compared to the bulk flow region. This indicates that the dynamic structuring of liquid argon and the interactions between carbon-argon molecules induce that

higher local viscosity in the interfacial region. In this capacity, these liquid layers act as an extended wall

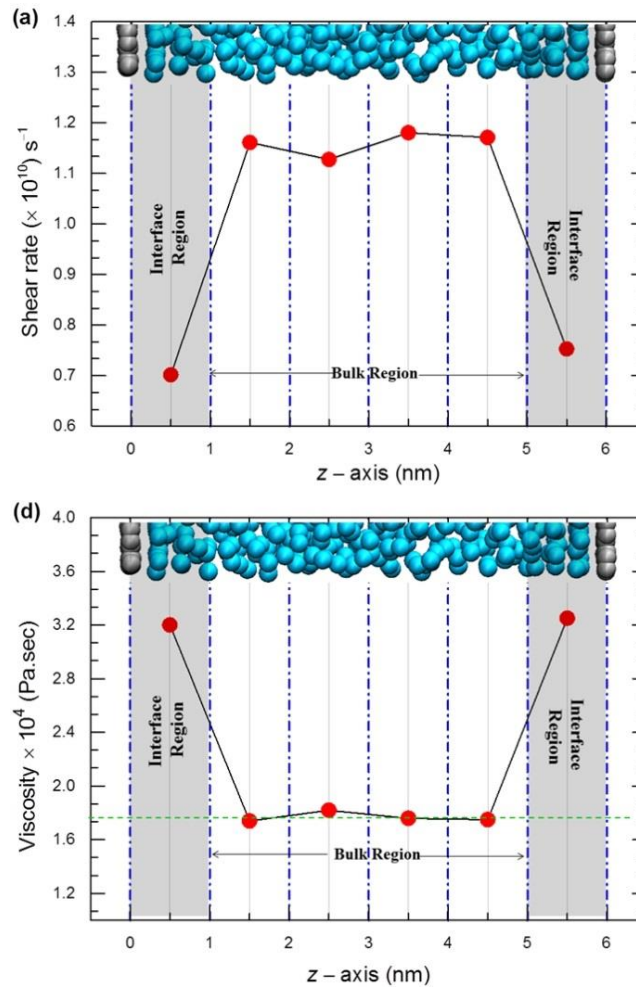


Figure 3.7. Distribution of (a) the shear rate ($\dot{\gamma} = \frac{dv_x}{dz}$) and (b) Local viscosity of liquid argon as a result of the sheared driven flow by the graphene walls

layer, which induces increased shearing in the middle of the fluid by reducing the width of the flow region. In nanoscale fluidic transport, such small variations at the interface have a significant effect on the flow characteristics. We also measure the S_{xz} and γ at the different wall/fluid boundary defined in figure 5c and observed an equivalent ratio for all of the cases.

3.5.1.4 Slip velocity inside graphene nanopore

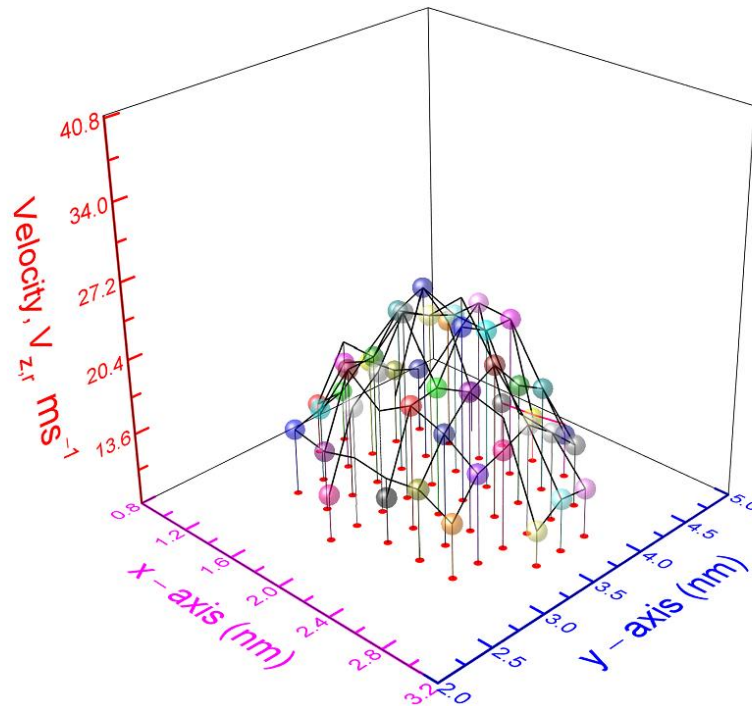


Figure 3.8. 3D averaged argon velocity profile in the radial direction (xy - plane) within $a_{cc} = 1.10925$ nm pore radius at $U_w = 3.5$ m/sec

In figure-3.8, the 3-dimensional averaged velocity profile resembles a hyperbolae shape of the Sampson flow through NPGM. In this case, spatial bin thickness of 0.25 nm in x - and y - directions, and 0.34 nm in z - direction was utilized only in the portion of graphene pore. Overall, velocity data of 21 argon molecules were averaged for 1 ns during an instantaneous course of simulation time at $U_w = 3.5$ m/sec. It was observed that the velocity of liquid argon molecules near the edge of pore was relatively slower than pore center suggesting the fluid layering effect inside graphene nanopore. Therefore, the first averaged velocity adjacent to the pore edge was considered as slip velocity (u_s). For better statistical accuracy and axisymmetric geometry of the nanopore, the velocity profile of liquid argon was computed utilizing cylindrical bin whose radius corresponds to the pore radius ($a_{cc} = 1.196$ nm) and bin length $\Delta z = 0.34$ nm as shown in figure 3.9. The cylindrical bin axis was

oriented along the z-direction of the pore center. To get the velocity data in the radial direction of the pore, the cylindrical bin also divided into 5, 8 and 10 concentric circle bin from the cylinder axis. Then the NEMD data from these three concentric circle bins, during different instantaneous simulation time, was averaged to finalize the argon velocity profile inside graphene nanopore. Primarily, the wall/liquid boundary inside nanopore was considered at three probable positions, (1) pore center to atomic center of carbon atoms at the pore edge (L), (2) pore center to density peak position of argon inside the pore region (L'), and (3) mean position of L and L' , where $L'' = \frac{L+L'}{2}$. The peak density position of argon inside the nanopore was considered where highest number of argon molecules was found in concentric circle bin. Thus, the boundary position for L' was located at 0.797 ± 0.0364 nm. In addition, the slip velocity was calculated 4.326 ± 0.378 m/sec at L and L'' , however, this value slightly increases about 5.55 ± 0.214 m/sec at L' boundary position in case of $U_w = 1.5$ m/sec.

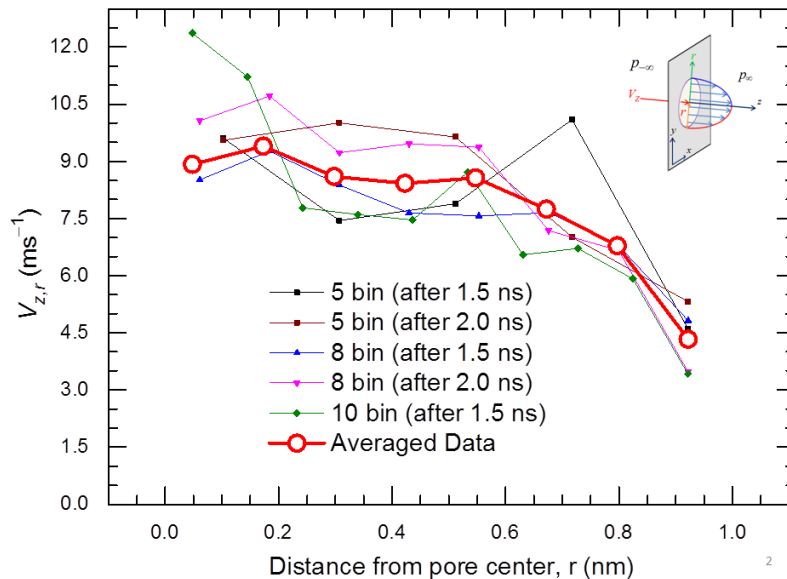


Figure 3.9. Argon velocity profile in the nanopore within $a_{CC} = 1.10925$ nm pore radius at $U_w = 1.5$ m/sec

We also observe that the slip velocity linearly increases with the increase of flow velocity depending on the location of wall/liquid boundary.

3.5.2 Comparison of continuum and molecular-level transport properties correlated with the definition of wall/liquid boundary near the pore edge

Figure 3.10 represents the comparison between the prediction of argon velocity from NEMD simulation and slip modified Sampson flow equation at $U_w = 1.5$ and 3.5 m/sec. Firstly, the pore radius $a_{cc} = 1.10925$ nm and bulk viscosity of argon were remained constant, while the pressure difference in the bulk and interface region was employed in eq5 as shown in figure 3.10(a–b). It is evident that the NEMD velocity profile is slower than the prediction of slip modified continuum velocity profile. This indicates that when argon molecules enter into the interfacial region from bulk flow region, the interaction strength between carbon-argon molecules reduces the argon velocity. In addition to that, with the increase of flow velocity, interface pressure difference provides a better flow prediction. Since, $P_{back,peak}$ remains unchanged, $P_{front,peak}$ should be increased by increasing the flow velocity for higher permeation rate of liquid through nanoporous membrane. Secondly, from figure 3.10(c–d) it is evident that the prediction from eq5 with μ_{int} provides better agreement to the MD liquid flow than μ_{bulk} irrespective of either pressure difference. This signifies that the increased viscosity near the interfacial region, due to the dynamic liquid structuring at the solid/liquid interface, created another energy barrier that needs to overcome by argon molecules for the permeation through graphene nanopore. Therefore, it is now clear that the continuum assumptions of Sampson flow equation completely break down at the molecular level fluidic transport for the inhomogeneous characteristics of fluid near the solid/liquid interface.

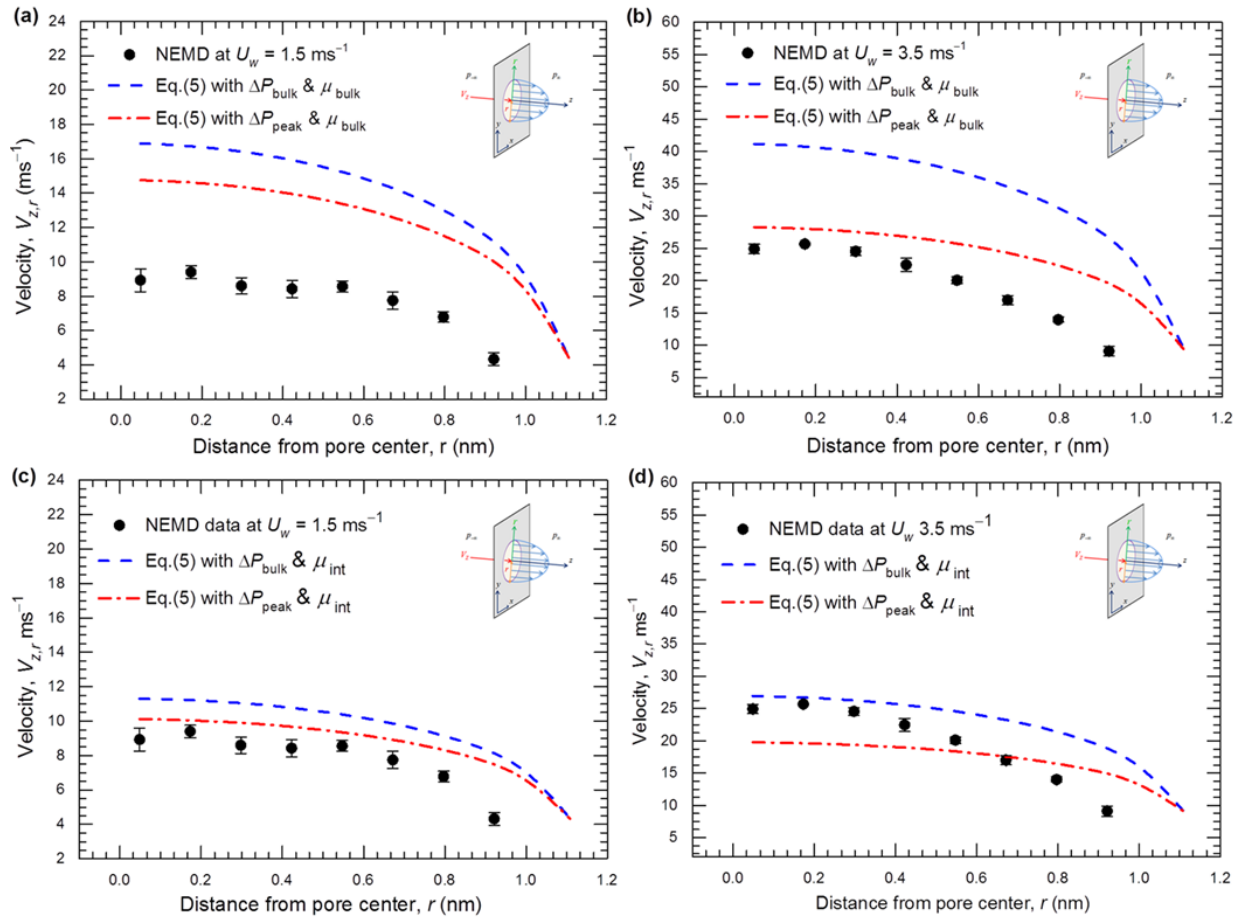


Figure 3.10. Comparison of velocity profile from NEMD simulations and modified Sampson flow equation within $a_{CC} = 1.10925$ nm pore radius by the varying pressure difference in bulk and interface region (a-b) with bulk viscosity, and (c-d) with interface viscosity at $U_w = 1.5$ and 3.5 m/sec

Finally, the location of wall/fluid boundary at the pore edge was analyzed with respect to μ_{int} and ΔP_{peak} in case of pore radius $a_{CC} = 1.10925$ nm, as shown in figure 3.11. Clearly, eq5 with the pore boundary position L provides a poor prediction of velocity profile as compared to the NEMD simulation. This is because the repulsive forces between particles near the wall/liquid boundary create a depletion space immediately adjacent to the solid wall. Hence, the exact volume occupied by argon molecules in confined channel slightly decreases which have a significant effect in the calculation velocity profile in nanometer range scale.

Although the pore boundary with L' provides better prediction, the relative deviation between eq5 and NEMD data near the pore edge is large. This implies that the exact pore boundary should be in between L and L' . In that case, the mean of that two boundary position provides an excellent consistency in the prediction of velocity profile inside graphene nanopore.

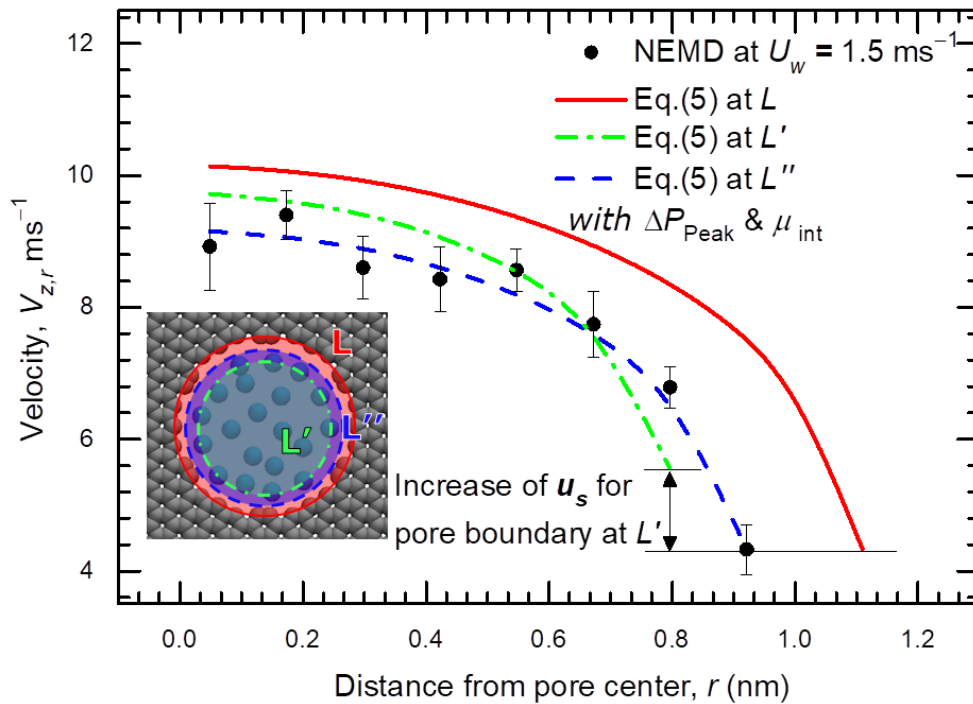


Figure 3.11. Comparison of velocity profile from NEMD simulations and modified Sampson flow equation for three probable pore boundary with ΔP_{peak} and μ_{int} at $U_w = 1.5$ m/sec. Data is obtained for $a_{cc} = 1.10925$ nm pore radius

Figure 3.12 represents the comparison between the prediction of argon velocity from NEMD simulation and slip modified Sampson flow equation with interfacial liquid dynamics properties at $U_w = 1.0$ to 2.5 m/sec. It is evident that eq5 with μ_{int} and ΔP_{peak} at pore boundary L'' exhibits excellent agreement with the NEMD data for low flow velocity. However, the

deviation in the velocity prediction started to increase for higher flow velocity. This is because the entrance interfacial pressure adjacent to the membrane increases with the increase of flow velocity. As a consequence, the shear stress between the argon and carbon molecules increases in that region, which further resists the argon molecules to overcome the increased free energy- barrier. Therefore, due the effect of nanoscale confinement, the local viscosity further needs to be correlated with the entrance interfacial pressure for increased flow velocity to more accurately predict the velocity profile inside graphene nanopore.

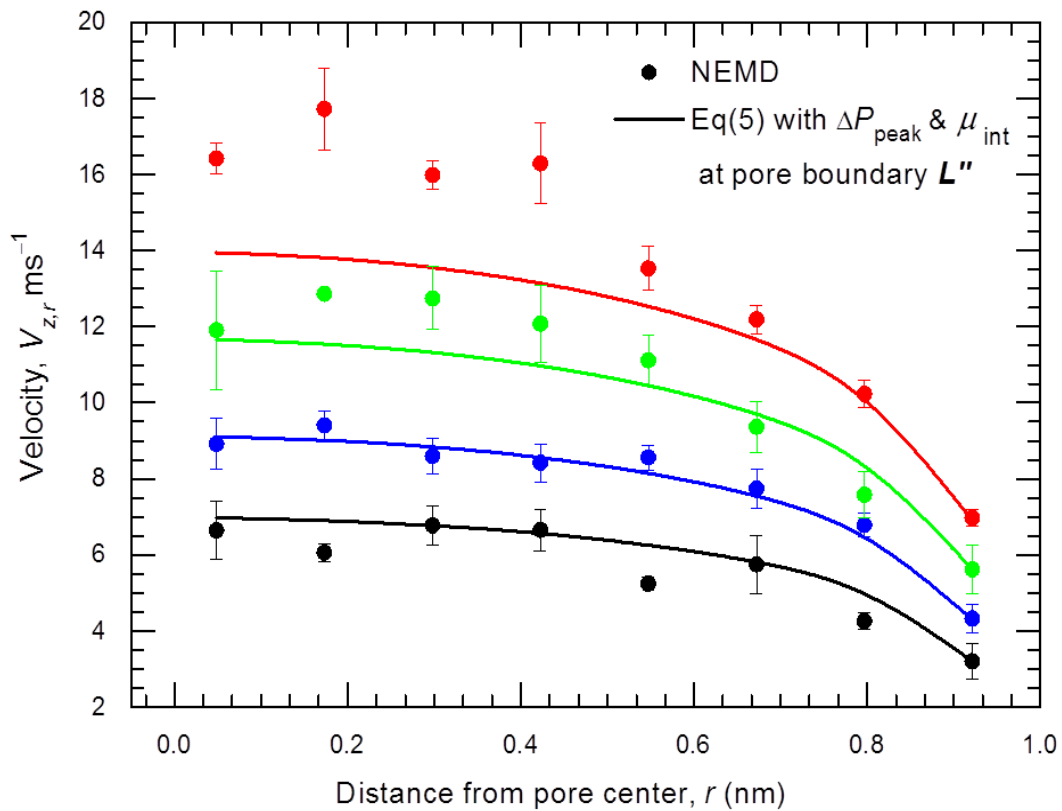


Figure 3.12. Comparison of velocity profile from NEMD simulations and modified Sampson flow equation for the pore boundary at L'' with ΔP_{peak} and μ_{int} . Each line and circle symbol profile with same color (from bottom) represents the data for $U_w = 1.0, 1.5, 2.0$ and 2.5 m/sec respectively. Data is obtained for $a_{cc} = 1.10925$ nm pore radius

3.6 Conclusion

In this study, we investigate the pressure-driven transport behavior of liquid argon through nanoporous graphene membrane using non-equilibrium molecular dynamics simulation. We observed layered density structure of liquid argon near the graphene membrane, which violates the incompressibility assumption of continuum description. The pressure difference was developed across the system by moving the specular reflection wall at constant velocity. Since the applied flow velocity doesn't change the molecular distribution in the respective flow region from their initial equilibrium configurations, the pressure difference is developed mainly due to the change in relative distance vector between the argon molecules from the SRW in the corresponding reservoir. Pressure at the interface region differs significantly from the bulk region because of fluid layering effect of argon molecules in the vicinity of graphene membrane. Based on the results, the interfacial pressure difference strongly depends on the intermolecular force of membrane governed by the layered structure of liquid and the applied flow velocity. In addition, argon velocity profile started to develop inside graphene nanopore until the bulk and peak pressure difference reaches to an equivalent value. From the shear driven flow simulation, we also observed higher local viscosity in the interfacial region than in the middle of the liquid flow. Argon velocity adjacent to the wall/fluid boundary near the pore edge was considered as slip velocity, and then, the Sampson flow equation was modified by adding the slip velocity into the continuum equation. By employing the characterized fluid dynamics properties on the slip modified continuum equation, we observed that the entrance interfacial pressure and higher local viscosity in the vicinity of graphene membrane associated with the optimized definition of wall/fluid boundary near the pore edge play a critical role for the permeation of argon through NPGM. Based on the results, the entry of argon into the nanopore is becoming energetically unfavorable, since the entrance interfacial pressure increases for increased flow

velocity. In contrary, the exit interfacial pressure remains unchanged indicating the marginal contribution to the free energy-barrier. Besides, the increased viscosity near the interfacial region created another energy barrier that needs to overcome by argon molecules for the permeation through graphene nanopore. For increased flow velocity, this local viscosity near the interfacial region should be further correlated with the entrance interfacial pressure for better flow prediction. In addition to that, the pressure on the interface could be affected depending on the ratio of pore area and total membrane area. This might also affect the stability of the membrane and velocity of simple liquid inside the nanopore for certain flow velocity. Hence, further examination of interfacial pressure based on the variation of total membrane area corresponding with certain pore area will be a part of our future research. Therefore, the effect of interfacial pressure near pore entrance, interface viscosity, slip velocity and the optimized definition of wall/fluid boundary should be carefully considered for the accurate prediction of fluid velocity inside graphene nanopore.

CHAPTER 4

Conclusions

In this thesis, I aim to understand the thermal and fluid transport mechanism at the molecular length scale by utilizing the equilibrium and non-equilibrium molecular dynamics simulations. From the obtained results, I explicitly analyze the structural and dynamic properties of fluid molecules at the solid/fluid interface. I also identify the limitations of the assumptions of continuum description and what factors mainly cause the deviation to the continuum transport theories in predicting fluid behaviors across nanoporous media.

The results presented in Chapter 2 demonstrate that the molecular weight of monolayer particles play a dominant factor in controlling the heat transport at the substrate/fluid interface. In case of heavier monolayer particles, the Kapitza resistance monotonically increases with increasing m_M , regardless of ϵ_{MM} . Because the vibrational mismatch between the particles at the interfacial region continuously increases with the subsequent addition of mass. On the other hand, for lighter monolayer particles, the interaction energy of monolayers is likely to maintain a better vibrational coupling with the solid substrate. Therefore, even if the vibrational mismatch marginally increases with the increase of m_M , ϵ_{MM} minimizes that mismatch which eventually leads to a reduced Kapitza resistance at the interfacial region.

In Chapter 3, I particularly characterize the local variations in fluid density, pressure, and viscosity across the simulation domain. I also calculate the three-dimensional velocity profile of argon inside graphene nanopore, while transporting through the membrane. The results reveal that the continuum flow equation associated with the interfacial fluid dynamics properties and proper wall/fluid boundary treatment inside graphene nanopore accurately

predicts the nanoscale fluid transport phenomena. Overall, the main reason of the deviation of fluid behavior from the continuum transport theories are are mainly due to (i) the interaction between wall and fluid molecules, (ii) the fluid layering effect at the interface region, (iii) slip velocity, (iv) entrance interfacial pressure, (v) local viscosity, and (vi) optimized wall/fluid boundary treatment at the interface.

REFERENCES

- [1] P.L. Kapitza, Heat Transfer and Superfluidity of Helium II, *Phys. Rev.* 60 (1941) 354–355.
- [2] L. Bocquet, E. Charlaix, Nanofluidics, from bulk to interfaces, *Chem. Soc. Rev.* 39 (2010) 1073–1095.
- [3] A.T. Pham, M. Barisik, B. Kim, Molecular dynamics simulations of Kapitza length for argon-silicon and water-silicon interfaces, *Int. J. Precis. Eng. Manuf.* 15 (2014) 323–329.
- [4] T.Q. Vo, B. Kim, Interface thermal resistance between liquid water and various metallic surfaces, *Int. J. Precis. Eng. Manuf.* 16 (2015) 1341–1346.
- [5] N. Asproulis, D. Drikakis, Boundary slip dependency on surface stiffness, *Phys. Rev. E.* 81 (2010) 061503.
- [6] N. Asproulis, D. Drikakis, Wall-mass effects on hydrodynamic boundary slip, *Phys. Rev. E.* 84 (2011) 031504.
- [7] J. Rafiee, X. Mi, H. Gullapalli, A.V. Thomas, F. Yavari, Y. Shi, P.M. Ajayan, N.A. Koratkar, Wetting transparency of graphene, *Nat Mater.* 11 (2012) 217–222.
- [8] A.T. Pham, M. Barisik, B. Kim, Interfacial thermal resistance between the graphene-coated copper and liquid water, *International Journal of Heat and Mass Transfer.* 97 (2016) 422–431.
- [9] P.K. Chow, E. Singh, B.C. Viana, J. Gao, J. Luo, J. Li, Z. Lin, A.L. Elías, Y. Shi, Z. Wang, M. Terrones, N. Koratkar, Wetting of Mono and Few-Layered WS₂ and MoS₂ Films Supported on Si/SiO₂ Substrates, *ACS Nano.* 9 (2015) 3023–3031.
- [10] T. Yamada, R. Matsuzaki, Effects of slit width on water permeation through graphene membrane by molecular dynamics simulations, *Sci Rep.* 8 (2018) 339.
- [11] M. Barisik, A. Beskok, Temperature dependence of thermal resistance at the water/silicon interface, *International Journal of Thermal Sciences.* 77 (2014) 47–54.
- [12] A. Pham, M. Barisik, B. Kim, Pressure dependence of Kapitza resistance at gold/water and silicon/water interfaces, *J. Chem. Phys.* 139 (2013) 244702.
- [13] C.T. Nguyen, M. Barisik, B. Kim, Wetting of chemically heterogeneous striped surfaces: Molecular dynamics simulations, *AIP Advances.* 8 (2018) 065003.
- [14] R.F. Hainsey, R. Gangwar, J.D. Shindler, R.M. Suter, Reentrant disordered phase in two-layer films of Kr on graphite, *Phys. Rev. B.* 44 (1991) 3365–3368.

- [15] L. Cheng, P. Fenter, K.L. Nagy, M.L. Schlegel, N.C. Sturchio, Molecular-Scale Density Oscillations in Water Adjacent to a Mica Surface, *Phys. Rev. Lett.* 87 (2001) 156103.
- [16] B.H. Kim, A. Beskok, T. Cagin, Molecular dynamics simulations of thermal resistance at the liquid-solid interface, *J. Chem. Phys.* 129 (2008) 174701.
- [17] B.H. Kim, A. Beskok, T. Cagin, Viscous heating in nanoscale shear driven liquid flows, *Microfluid Nanofluid.* 9 (2010) 31–40.
- [18] Q.V. Dinh, T.Q. Vo, B. Kim, Viscous heating and temperature profiles of liquid water flows in copper nanochannel, *J Mech Sci Technol.* 33 (2019) 3257–3263.
- [19] T.Q. Vo, B. Kim, Transport Phenomena of Water in Molecular Fluidic Channels, *Scientific Reports.* 6 (2016) 33881.
- [20] S. Plimpton, Fast Parallel Algorithms for Short-Range Molecular Dynamics, *Journal of Computational Physics.* 117 (1995) 1–19.
- [21] P.A. Thompson, S.M. Troian, A general boundary condition for liquid flow at solid surfaces, *Nature.* 389 (1997) 360–362.
- [22] G.E. Karniadakis, A. Beskok, N. Aluru, *Microflows and Nanoflows: Fundamentals and Simulation*, Springer-Verlag, New York, 2005.
- [23] D.G. Cahill, P.V. Braun, G. Chen, D.R. Clarke, S. Fan, K.E. Goodson, P. Koblinski, W.P. King, G.D. Mahan, A. Majumdar, H.J. Maris, S.R. Phillpot, E. Pop, L. Shi, Nanoscale thermal transport. II. 2003–2012, *Applied Physics Reviews.* 1 (2014) 011305.
- [24] H. Han, S. Mérabia, F. Müller-Plathe, Thermal Transport at Solid–Liquid Interfaces: High Pressure Facilitates Heat Flow through Nonlocal Liquid Structuring, *J. Phys. Chem. Lett.* 8 (2017) 1946–1951.
- [25] T. Ohara, D. Torii, Molecular dynamics study of thermal phenomena in an ultrathin liquid film sheared between solid surfaces: The influence of the crystal plane on energy and momentum transfer at solid-liquid interfaces, *J. Chem. Phys.* 122 (2005) 214717.
- [26] A.R. bin Saleman, H.K. Chilukoti, G. Kikugawa, M. Shibahara, T. Ohara, A molecular dynamics study on the thermal transport properties and the structure of the solid–liquid interfaces between face centered cubic (FCC) crystal planes of gold in contact with linear alkane liquids, *International Journal of Heat and Mass Transfer.* 105 (2017) 168–179.
- [27] Z. Shi, M. Barisik, A. Beskok, Molecular dynamics modeling of thermal resistance at argon-graphite and argon-silver interfaces, *International Journal of Thermal Sciences.* 59 (2012) 29–37.

- [28] H. Han, S. Merabia, F. Müller-Plathe, Thermal transport at a solid–nanofluid interface: from increase of thermal resistance towards a shift of rapid boiling, *Nanoscale*. 9 (2017) 8314–8320.
- [29] P. Keblinski, S.R. Phillpot, S.U.S. Choi, J.A. Eastman, Mechanisms of heat flow in suspensions of nano-sized particles (nanofluids), *International Journal of Heat and Mass Transfer*. 45 (2002) 855–863.
- [30] H. Hu, Y. Sun, Effect of nanopatterns on Kapitza resistance at a water-gold interface during boiling: A molecular dynamics study, *Journal of Applied Physics*. 112 (2012) 053508.
- [31] Y. Wang, P. Keblinski, Role of wetting and nanoscale roughness on thermal conductance at liquid-solid interface, *Appl. Phys. Lett.* 99 (2011) 073112.
- [32] K.M. Issa, A.A. Mohamad, Lowering liquid-solid interfacial thermal resistance with nanopatterned surfaces, *Phys. Rev. E*. 85 (2012) 031602.
- [33] T.Q. Vo, B. Kim, Physical origins of temperature continuity at an interface between a crystal and its melt, *J. Chem. Phys.* 148 (2018) 034703.
- [34] T.Q. Vo, M. Barisik, B. Kim, Near-surface viscosity effects on capillary rise of water in nanotubes, *Phys. Rev. E*. 92 (2015) 053009.
- [35] S. Becker, H.M. Urbassek, M. Horsch, H. Hasse, Contact Angle of Sessile Drops in Lennard-Jones Systems, *Langmuir*. 30 (2014) 13606–13614.
- [36] M. Barisik, A. Beskok, Wetting characterisation of silicon (1,0,0) surface, *Molecular Simulation*. 39 (2013) 700–709.
- [37] T.Q. Vo, B. Kim, Interface thermal resistance between liquid water and various metallic surfaces, *Int. J. Precis. Eng. Manuf.* 16 (2015) 1341–1346.
- [38] B. Kim, Thermal resistance at a liquid–solid interface dependent on the ratio of thermal oscillation frequencies, *Chemical Physics Letters*. 554 (2012) 77–81.
- [39] J.-L. BARRAT, F. CHIARUTTINI, Kapitza resistance at the liquid—solid interface, *Molecular Physics*. 101 (2003) 1605–1610.
- [40] J. Ghorbanian, A. Beskok, Temperature profiles and heat fluxes observed in molecular dynamics simulations of force-driven liquid flows, *Phys. Chem. Chem. Phys.* 19 (2017) 10317–10325.
- [41] J. Ghorbanian, A.T. Celebi, A. Beskok, A phenomenological continuum model for force-driven nano-channel liquid flows, *J. Chem. Phys.* 145 (2016) 184109.

- [42] T.Q. Vo, B. Park, C. Park, B. Kim, Nano-scale liquid film sheared between strong wetting surfaces: effects of interface region on the flow, *J Mech Sci Technol.* 29 (2015) 1681–1688.
- [43] A.S. Tascini, J. Armstrong, E. Chiavazzo, M. Fasano, P. Asinari, F. Bresme, Thermal transport across nanoparticle–fluid interfaces: the interplay of interfacial curvature and nanoparticle–fluid interactions, *Phys. Chem. Chem. Phys.* 19 (2017) 3244–3253.
- [44] Z. Ge, D.G. Cahill, P.V. Braun, Thermal Conductance of Hydrophilic and Hydrophobic Interfaces, *Phys. Rev. Lett.* 96 (2006) 186101.
- [45] K.S. Novoselov, A.K. Geim, S.V. Morozov, D. Jiang, Y. Zhang, S.V. Dubonos, I.V. Grigorieva, A.A. Firsov, Electric Field Effect in Atomically Thin Carbon Films, *Science.* 306 (2004) 666–669.
- [46] R. Mas-Ballesté, C. Gómez-Navarro, J. Gómez-Herrero, F. Zamora, 2D materials: to graphene and beyond, *Nanoscale.* 3 (2011) 20–30.
- [47] D. Akinwande, C.J. Brennan, J.S. Bunch, P. Egberts, J.R. Felts, H. Gao, R. Huang, J.-S. Kim, T. Li, Y. Li, K.M. Liechti, N. Lu, H.S. Park, E.J. Reed, P. Wang, B.I. Yakobson, T. Zhang, Y.-W. Zhang, Y. Zhou, Y. Zhu, A review on mechanics and mechanical properties of 2D materials—Graphene and beyond, *Extreme Mechanics Letters.* 13 (2017) 42–77.
- [48] J. Rafiee, X. Mi, H. Gullapalli, A.V. Thomas, F. Yavari, Y. Shi, P.M. Ajayan, N.A. Koratkar, Wetting transparency of graphene, *Nature Mater.* 11 (2012) 217–222.
- [49] D.J. Preston, D.L. Mafra, N. Miljkovic, J. Kong, E.N. Wang, Scalable Graphene Coatings for Enhanced Condensation Heat Transfer, *Nano Lett.* 15 (2015) 2902–2909.
- [50] B. Ramos-Alvarado, S. Kumar, G.P. Peterson, Solid–Liquid Thermal Transport and Its Relationship with Wettability and the Interfacial Liquid Structure, *J. Phys. Chem. Lett.* 7 (2016) 3497–3501.
- [51] R.J. Stevens, L.V. Zhigilei, P.M. Norris, Effects of temperature and disorder on thermal boundary conductance at solid–solid interfaces: Nonequilibrium molecular dynamics simulations, *International Journal of Heat and Mass Transfer.* 50 (2007) 3977–3989.
- [52] S. Merabia, K. Termentzidis, Thermal conductance at the interface between crystals using equilibrium and nonequilibrium molecular dynamics, *Phys. Rev. B.* 86 (2012) 094303.
- [53] Z. Liang, H.-L. Tsai, Effect of thin film confined between two dissimilar solids on interfacial thermal resistance, *J. Phys.: Condens. Matter.* 23 (2011) 495303.

- [54] Z. Liang, H.-L. Tsai, Reduction of solid–solid thermal boundary resistance by inserting an interlayer, *International Journal of Heat and Mass Transfer*. 55 (2012) 2999–3007.
- [55] M.P. Allen, D.J. Tildesley, *Computer Simulation of Liquids: Second Edition*, Oxford University Press, 2017.
- [56] J.H. Irving, J.G. Kirkwood, The Statistical Mechanical Theory of Transport Processes. IV. The Equations of Hydrodynamics, *J. Chem. Phys.* 18 (1950) 817–829.
- [57] B.D. Todd, P.J. Davis, D.J. Evans, Heat flux vector in highly inhomogeneous nonequilibrium fluids, *Phys. Rev. E*. 51 (1995) 4362–4368.
- [58] A.J.H. McGaughey, M. Kaviani, Thermal conductivity decomposition and analysis using molecular dynamics simulations. Part I. Lennard-Jones argon, *International Journal of Heat and Mass Transfer*. 47 (2004) 1783–1798.
- [59] B.J. Bailey, K. Kellner, The thermal conductivity of liquid and gaseous argon, *Physica*. 39 (1968) 444–462.
- [60] H. Ziebland, J.T.A. Burton, The thermal conductivity of nitrogen and argon in the liquid and gaseous states, *Br. J. Appl. Phys.* 9 (1958) 52–59.
- [61] B.H. Kim, A. Beskok, T. Cagin, Thermal interactions in nanoscale fluid flow: molecular dynamics simulations with solid–liquid interfaces, *Microfluid Nanofluid*. 5 (2008) 551–559.
- [62] L. Xue, P. Keblinski, S.R. Phillpot, S.U.-S. Choi, J.A. Eastman, Effect of liquid layering at the liquid–solid interface on thermal transport, *International Journal of Heat and Mass Transfer*. 47 (2004) 4277–4284.
- [63] M. Frank, M. Kio, D. Drikakis, L. Könözy, N. Asproulis, Mass and Stiffness Effects on Thermal Resistance at the Solid–Liquid Interface of Nanofluidic Channels, (2018).
- [64] E.T. Swartz, R.O. Pohl, Thermal boundary resistance, *Rev. Mod. Phys.* 61 (1989) 605–668.
- [65] R.W. Baker, B.T. Low, Gas Separation Membrane Materials: A Perspective, *Macromolecules*. 47 (2014) 6999–7013.
- [66] A. Tavolaro, E. Drioli, Zeolite Membranes, *Advanced Materials*. 11 (1999) 975–996.
- [67] H. Furukawa, K.E. Cordova, M. O’Keeffe, O.M. Yaghi, The chemistry and applications of metal-organic frameworks, *Science*. 341 (2013) 1230444.
- [68] L. Wang, M.S.H. Boutilier, P.R. Kidambi, D. Jang, N.G. Hadjiconstantinou, R. Karnik, Fundamental transport mechanisms, fabrication and potential applications of nanoporous atomically thin membranes, *Nat Nanotechnol*. 12 (2017) 509–522.

- [69] J.K. Holt, H.G. Park, Y. Wang, M. Stadermann, A.B. Artyukhin, C.P. Grigoropoulos, A. Noy, O. Bakajin, Fast mass transport through sub-2-nanometer carbon nanotubes, *Science*. 312 (2006) 1034–1037.
- [70] M. Majumder, N. Chopra, R. Andrews, B.J. Hinds, Enhanced flow in carbon nanotubes, *Nature*. 438 (2005) 44–44.
- [71] G. Hummer, J.C. Rasaiah, J.P. Noworyta, Water conduction through the hydrophobic channel of a carbon nanotube, *Nature*. 414 (2001) 188–190.
- [72] A.I. Skoulidas, D.M. Ackerman, J.K. Johnson, D.S. Sholl, Rapid Transport of Gases in Carbon Nanotubes, *Phys. Rev. Lett.* 89 (2002) 185901.
- [73] C. Lee, X. Wei, J.W. Kysar, J. Hone, Measurement of the elastic properties and intrinsic strength of monolayer graphene, *Science*. 321 (2008) 385–388.
- [74] O. Eksik, S.F. Bartolucci, T. Gupta, H. Fard, T. Borca-Tasciuc, N. Koratkar, A novel approach to enhance the thermal conductivity of epoxy nanocomposites using graphene core–shell additives, *Carbon*. 101 (2016) 239–244.
- [75] E. Pop, V. Varshney, A.K. Roy, Thermal properties of graphene: Fundamentals and applications, *MRS Bulletin*. 37 (2012) 1273–1281.
- [76] A.V. Thomas, B.C. Andow, S. Suresh, O. Eksik, J. Yin, A.H. Dyson, N. Koratkar, Controlled crumpling of graphene oxide films for tunable optical transmittance, *Adv. Mater. Weinheim*. 27 (2015) 3256–3265.
- [77] A.K. Geim, K.S. Novoselov, The rise of graphene, *Nature Mater.* 6 (2007) 183–191.
- [78] C.-J. Shih, Q.H. Wang, S. Lin, K.-C. Park, Z. Jin, M.S. Strano, D. Blankschtein, Breakdown in the Wetting Transparency of Graphene, *Phys. Rev. Lett.* 109 (2012) 176101.
- [79] D. Ghoshal, R. Jain, N.A. Koratkar, Graphene’s Partial Transparency to van der Waals and Electrostatic Interactions, *Langmuir*. 35 (2019) 12306–12316.
- [80] S.C. O’Hern, M.S.H. Boutilier, J.-C. Idrobo, Y. Song, J. Kong, T. Laoui, M. Atieh, R. Karnik, Selective ionic transport through tunable subnanometer pores in single-layer graphene membranes, *Nano Lett.* 14 (2014) 1234–1241.
- [81] M.A. Shannon, P.W. Bohn, M. Elimelech, J.G. Georgiadis, B.J. Mariñas, A.M. Mayes, Science and technology for water purification in the coming decades, *Nature*. 452 (2008) 301–310.
- [82] S. Ghosh, A.K. Sood, N. Kumar, Carbon Nanotube Flow Sensors, *Science*. 299 (2003) 1042–1044.

- [83] S.J. Peighambaroust, S. Rowshanzamir, M. Amjadi, Review of the proton exchange membranes for fuel cell applications, *International Journal of Hydrogen Energy*. 35 (2010) 9349–9384.
- [84] T. Palaniselvam, V. Kashyap, S.N. Bhange, J.-B. Baek, S. Kurungot, Nanoporous Graphene Enriched with Fe/Co-N Active Sites as a Promising Oxygen Reduction Electrocatalyst for Anion Exchange Membrane Fuel Cells, *Advanced Functional Materials*. 26 (2016) 2150–2162.
- [85] R.H. Tunuguntla, F.I. Allen, K. Kim, A. Belliveau, A. Noy, Ultrafast proton transport in sub-1-nm diameter carbon nanotube porins, *Nature Nanotechnology*. 11 (2016) 639–644.
- [86] D. Konatham, J. Yu, T.A. Ho, A. Striolo, Simulation Insights for Graphene-Based Water Desalination Membranes, *Langmuir*. 29 (2013) 11884–11897.
- [87] D. Cohen-Tanugi, J.C. Grossman, Water Desalination across Nanoporous Graphene, *Nano Lett.* 12 (2012) 3602–3608.
- [88] D. Cohen-Tanugi, J.C. Grossman, Water permeability of nanoporous graphene at realistic pressures for reverse osmosis desalination, *J. Chem. Phys.* 141 (2014) 074704.
- [89] M.E. Suk, N.R. Aluru, Water Transport through Ultrathin Graphene, *J. Phys. Chem. Lett.* 1 (2010) 1590–1594.
- [90] M.E. Suk, N.R. Aluru, Molecular and continuum hydrodynamics in graphene nanopores, *RSC Adv.* 3 (2013) 9365–9372.
- [91] K. Sint, B. Wang, P. Král, Selective Ion Passage through Functionalized Graphene Nanopores, *J. Am. Chem. Soc.* 130 (2008) 16448–16449.
- [92] M.E. Suk, N.R. Aluru, Ion transport in sub-5-nm graphene nanopores, *J. Chem. Phys.* 140 (2014) 084707.
- [93] S. Zhao, J. Xue, W. Kang, Ion selection of charge-modified large nanopores in a graphene sheet, *J. Chem. Phys.* 139 (2013) 114702.
- [94] C.T. Nguyen, A. Beskok, Saltwater transport through pristine and positively charged graphene membranes, *J. Chem. Phys.* 149 (2018) 024704.
- [95] C.T. Nguyen, A. Beskok, Charged nanoporous graphene membranes for water desalination, *Phys. Chem. Chem. Phys.* 21 (2019) 9483–9494.
- [96] R.A. Sampson, A.G. Greenhill, XII. On Stokes's current function, *Philosophical Transactions of the Royal Society of London. (A.)*. 182 (1891) 449–518.

- [97] R.R. Ph.D, XXXI. The flow of viscous fluids round plane obstacles, The London, Edinburgh, and Dublin Philosophical Magazine and Journal of Science. 40 (1949) 338–351.
- [98] H.L. Weissberg, End Correction for Slow Viscous Flow through Long Tubes, The Physics of Fluids. 5 (1962) 1033–1036.
- [99] Z. Dagan, S. Weinbaum, R. Pfeffer, An infinite-series solution for the creeping motion through an orifice of finite length, Journal of Fluid Mechanics. 115 (1982) 505–523.
- [100] J.-L. Barrat, L. Bocquet, Large Slip Effect at a Nonwetting Fluid-Solid Interface, Phys. Rev. Lett. 82 (1999) 4671–4674.
- [101] N.V. Priezjev, A.A. Darhuber, S.M. Troian, Slip behavior in liquid films on surfaces of patterned wettability: Comparison between continuum and molecular dynamics simulations, Phys. Rev. E. 71 (2005) 041608.
- [102] M.R. Hasan, T.Q. Vo, B. Kim, Manipulating thermal resistance at the solid–fluid interface through monolayer deposition, RSC Adv. 9 (2019) 4948–4956.
- [103] X. Chen, G. Cao, A. Han, V.K. Punyamurtula, L. Liu, P.J. Culligan, T. Kim, Y. Qiao, Nanoscale Fluid Transport: Size and Rate Effects, Nano Lett. 8 (2008) 2988–2992.
- [104] J. Koplik, J.R. Banavar, J.F. Willemsen, Molecular dynamics of fluid flow at solid surfaces, Physics of Fluids A: Fluid Dynamics. 1 (1989) 781–794.
- [105] R. Bhaduria, N.R. Aluru, A quasi-continuum hydrodynamic model for slit shaped nanochannel flow, J. Chem. Phys. 139 (2013) 074109.
- [106] J.A. Thomas, A.J.H. McGaughey, Reassessing Fast Water Transport Through Carbon Nanotubes, Nano Lett. 8 (2008) 2788–2793.
- [107] T.S. Ingebrigtsen, T.B. Schrøder, J.C. Dyre, What Is a Simple Liquid?, Phys. Rev. X. 2 (2012) 011011.
- [108] L. Bøhling, T.S. Ingebrigtsen, A. Grzybowski, M. Paluch, J.C. Dyre, T.B. Schrøder, Scaling of viscous dynamics in simple liquids: theory, simulation and experiment, New J. Phys. 14 (2012) 113035.
- [109] K.H. Jensen, A.X.C.N. Valente, H.A. Stone, Flow rate through microfilters: Influence of the pore size distribution, hydrodynamic interactions, wall slip, and inertia, Physics of Fluids. 26 (2014) 052004.
- [110] N.B. Vargaftik, Handbook of Physical Properties of Liquids and Gases: Pure Substances and Mixtures, 2nd ed., Springer-Verlag, Berlin Heidelberg, 1975.

MOHAMMAD RASHEDUL HASAN

Micro/Nano-scale Thermo-Fluids
Engineering Lab.
University of Ulsan 93 Daehak-ro, Nam-gu
Ulsan (44610), South Korea

Email: rashedulhasan.047@gmail.com

Last Update: 29 November 2019

RESEARCH INTERESTS

- **Fundamental/Theory:** Interfacial Phenomena, Multi-scale Modeling (Nanoscale – Continuum), Nanofluidics, Statistical Thermodynamics, Molecular Dynamics Simulation
- **Applications:** Water Desalination, Energy Storage Device, Hydrogen Fuel Cell, Thermal Management

EDUCATION

- **University of Ulsan, South Korea** September 2017 – February 2020
MSc in Mechanical Engineering
CGPA: **4.44/4.50 (99.31% Marks)**
- **Khulna University of Engineering & Technology, Bangladesh** March 2010 – July 2014
BSc in Mechanical Engineering

RESEARCH EXPERIENCE

- **Graduate Research Assistant** in Micro/Nano-scale Thermo-Fluids Engineering Lab. (September 2017–December 2020), University of Ulsan, South Korea
Research Advisor: Dr. BoHung Kim
Analysis Technique: Molecular Dynamics Simulation (EMD & NEMD)
Performed analysis: Interfacial phenomena (Interfacial thermal resistance, Liquid layering, Temperature Jump, Shear Viscosity, velocity Slip Length), Thermodynamics properties (Density, Pressure, Temperature, Viscosity and Thermal Conductivity), Local Thermodynamics Equilibrium (Maxwell-Boltzmann Distribution), Vibrational Density of States, Flow Modeling (Shear driven, Force driven and Flow in nanopore), Green-Kubo method
- **Undergraduate Research Student** in Aerodynamics Lab. (June 2013 – July 2014), Khulna University of Engineering & Technology, Bangladesh
Research Advisor: Dr. Mohammad Mashud
Performed analysis: Lift and Drag co-efficient in Airfoil, Power-coefficient in Wind Turbine

RESEARCH PROJECT

- **Manipulating thermal resistance at the solid–fluid interface through monolayer deposition**

At the interface between monolayer coated solid substrate and fluid, the effect of interfacial mismatch on Kapitza length due to the monolayer particles has been extensively analyzed through a series of non-equilibrium molecular dynamics simulation.

- **Nanopore Flow Modeling for Water Desalination**

In this study, we investigated the transport mechanisms of ions and water through graphene nanopore. To quantify the transport behavior, we measured the hydrodynamics properties such as water flux, pressure and density distribution, velocity along the radial direction of pore, local viscosity. In the end, we modified the continuum flow equation from the obtained hydrodynamics properties by using non-equilibrium molecular dynamics simulation.

SKILLS

- Molecular Modeling: Material Studio, LAMMPS
- Molecular Analysis: LAMMPS
- CFD Analysis: Ansys FLUENT
- Visualization: OVITO, VMD
- Post-processing: Origin, MATLAB Plot
- Design: Solidworks, AutoCad

JOURNAL PUBLICATIONS

- **Hasan, Mohammad Rashedul**, Truong Quoc Vo, and BoHung Kim. "*Manipulating thermal resistance at the solid–fluid interface through monolayer deposition.*" **RSC Advances** 9, no. 9 (2019): 4948-4956.

PROCEEDING PAPERS

- **MR Hasan**, Md. R Islam, GMH Shahariar, M Mashud, "*Numerical analysis of vertical axis wind turbine*", IEEE Xplore, DOI: 10.1109/IFOST.2014.6991130
- GMH Shahariar, **MR Hasan**, "*Design & Construction of a Vertical Axis Wind Turbine*", IEEE Xplore, DOI: 10.1109/IFOST.2014.6991132

JOURNAL UNDER PREPERATION

- **Mohammad Rashedul Hasan**, BoHung Kim, "*Nanopore Flow Modeling for the Transportation of argon through Nanoporous Graphene*", 2019.

CONFERENCE PRESENTATIONS

- BoHung Kim*, **Mohammad Rashedul Hasan**, "Nanoscale Thermal Resistance at the Dissimilar Material Interface for the Additive Manufacturing", International

Symposium on PReCISION Engineering and Sustainable Manufacturing (PRESM), Vietnam (10–13 July, 2019) **(Oral)**

- **Mohammad Rashedul Hasan***, BoHung Kim, “Nanopore Flow Modeling for the Transportation of Water through Nanoporous Graphene”, The Korean Society of Mechanical Engineers (KSME) Ulsan branch, South Korea (24 May, 2019) **(Oral)**
- **MR Hasan***, Md. R Islam, GMH Shahariar, M Mashud, “Numerical analysis of vertical axis wind turbine”, The 9th International Forum on Strategic Technology (IFOST), Bangladesh (21-23 November, 2014), **(Oral)**

TEST SCORE

- IELTS Overall score: **7.0**; Listening: 7.5; Reading: 8.0; Speaking: 6.0; Writing: 6.0 (Test Date: 13 April, 2019)
- GRE Revised score: 306 (Quantitative 157, Verbal 149, AWA 2.5)

SCHOLARSHIPS AND AWARDS

- **Mohammad Rashedul Hasan***, BoHung Kim, “Nanopore Flow Modeling for the Transportation of Water through Nanoporous Graphene”, The Korean Society of Mechanical Engineers (KSME) Ulsan branch, South Korea (24 May, 2019) **(Best Presentation Award)**
- AF-1 Scholarship (full tuition fee) awarded by Mechanical & Automotive Engineering Department, University of Ulsan and Research grant by National Research Foundation of Korea (NRF) (September 2017 ~ February 2020)
- Technical Scholarship supported by Bangladesh government: 2011, 2012, 2013